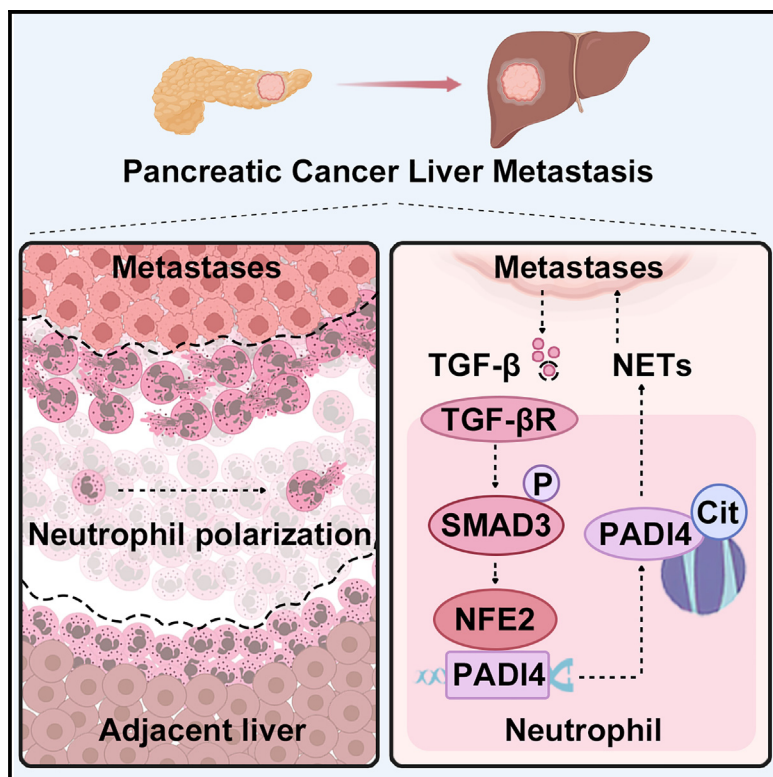


NFE2-driven neutrophil polarization promotes pancreatic cancer liver metastasis progression

Graphical abstract



Authors

Wencho Xu, Jianzhou Liu, Qiaofei Liu, ..., Bowen Huang, Gary Guishan Xiao, Junchao Guo

Correspondence

pumch_research@163.com

In brief

Xu et al. investigated the single-cell characteristics of pancreatic cancer liver metastasis and found that the pro-metastatic neutrophil cluster is enriched at the metastatic border. NFE2-driven neutrophil phenotypic polarization represents a critical pro-metastatic mechanism. TGF-β/SMAD3 activates NFE2, further promoting NET release at the invasive front by transcriptional regulation of PADI4.

Highlights

- Single-cell and spatial atlas of PCLM based on paired human samples
- Pro-metastatic neutrophil cluster is enriched at the metastatic invasive front
- NFE2 transcriptionally regulates PADI4 expression and promotes NET generation
- NFE2-driven neutrophil polarization toward pro-metastatic phenotype induced by TGF-β



Article

NFE2-driven neutrophil polarization promotes pancreatic cancer liver metastasis progression

Wenchao Xu,^{1,2,3,4,9} Jianzhou Liu,^{1,2,3,4,9} Qiaofei Liu,^{1,2,3,4} Jia Xu,⁵ Li Zhou,^{1,2,3,4} Zhiyong Liang,⁶ Haoran Huang,^{1,2,3,4,7} Bowen Huang,⁸ Gary Guishan Xiao,⁵ and Junchao Guo^{1,2,3,4,10,*}

¹Department of General Surgery, Peking Union Medical College Hospital, Chinese Academy of Medical Sciences and Peking Union Medical College, Beijing 100730, China

²Key Laboratory of Research in Pancreatic Tumor, Chinese Academy of Medical Sciences, Beijing 100730, China

³National Infrastructures for Translational Medicine, Peking Union Medical College Hospital, Beijing 100730, China

⁴State Key Laboratory of Complex, Severe, and Rare Diseases, Peking Union Medical College Hospital, Chinese Academy of Medical Sciences and Peking Union Medical College, Beijing 100730, China

⁵State Key Laboratory of Fine Chemicals, Department of Pharmaceutical Sciences, School of Chemical Engineering, Dalian University of Technology, Dalian 116024, China

⁶Department of Pathology, Molecular Pathology Research Centre, Peking Union Medical College Hospital, Chinese Academy of Medical Science and Peking Union Medical College, Beijing 100730, China

⁷School of Medicine, Tsinghua University, Beijing 100730, China

⁸Department of Gastric Surgery, Sun Yat-sen University Cancer Center, State Key Laboratory of Oncology in South China, Guangdong Provincial Clinical Research Center for Cancer, Guangzhou 510060, China

⁹These authors contributed equally

¹⁰Lead contact

*Correspondence: pumch_research@163.com

<https://doi.org/10.1016/j.celrep.2024.115226>

SUMMARY

Pancreatic cancer liver metastasis is an important factor leading to dismal prognoses. The details of adaptive immune remodeling in liver metastasis, especially the role of neutrophils, remain elusive. Here, combined single-cell sequencing with spatial transcriptomics results revealed that liver metastases exhibit more aggressive transcriptional characteristics and higher levels of immunosuppression compared with the primary tumor. We identified neutrophils_S100A12 (S100 calcium binding protein A12) cells as the pivotal pro-metastatic cluster, specifically distributed at the invasive front of the metastatic lesions. Mechanistically, our findings indicated that nuclear factor erythroid 2 (NFE2) is a key transcription factor regulating neutrophil phenotypic polarization. Metastatic tumors produce transforming growth factor β to activate the SMAD3 pathway within neutrophils, inducing NFE2-driven polarization. NFE2 promotes the transcription of peptidylarginine deiminase 4 by binding to its promoter, leading to the generation of neutrophil extracellular traps at the invasive front. Collectively, our data demonstrate that NFE2-driven neutrophil polarization is a potential target for anti-metastatic therapy.

INTRODUCTION

Liver metastasis (LM) is a significant barrier to extended survival in patients with pancreatic cancer (PC).¹ Many studies have explored the highly disseminated characteristics of malignant cells,^{2,3} while recent insights underscored the pivotal roles of the tumor microenvironment (TME) in facilitating tumor metastasis.^{4,5} The processes of remodeling the metastatic TME have already occurred in the target organ before the arrival of tumor cells.^{6,7} After colonization, metastatic tumors further alter the local TME to support their growth.^{8,9} However, the analysis and interpretation of the transcriptional heterogeneity and spatial characteristics of PCLM are very restricted, limiting the development of anti-metastatic strategies.

Massive infiltration of target organs by neutrophils is an essential feature of metastasis, and neutrophils are thought to accelerate metastasis progression.^{10,11} Differences in the density,

surface markers, and transcriptional characteristics of different neutrophil populations in tumors have been demonstrated, suggesting that neutrophils undergo functional differentiation during their involvement in tumor progression.^{12–14} However, the causes and characteristics of internal heterogeneity within neutrophils and the role of neutrophil phenotypic polarization in LM remain elusive.

Here, we performed a comprehensive analysis of paired primary and liver metastatic tumors obtained from surgical resection samples, employing a dual approach of single-cell RNA sequencing (scRNA-seq) and spatial transcriptomics (ST). Our findings revealed distinct transcriptional profiles and spatial variations of diverse cell types within primary tumors (PTs) and LMs. Specifically, we identified the functional diversity possessed by neutrophils in PCLM and demonstrated that a specific invasive zone at the front of the liver metastatic lesions was enriched with pro-metastatic neutrophils_S100A12 (S100 calcium binding



protein A12) cells. The liver metastatic tumor activates the transforming growth factor β (TGF- β)/SMAD3 signaling pathway within the infiltrating neutrophils, inducing nuclear factor erythroid 2 (NFE2)-driven pro-metastatic polarization. The activation of NFE2 upregulates peptidylarginine deiminase 4 (PAD4) expression, leading to the release of neutrophil extracellular traps (NETs) at the invasive front. In light of our findings, we propose that reversing the NFE2-driven functional reprogramming of neutrophils could be a potential strategy for anti-metastatic therapy.

RESULTS

Exploring the PCLM landscape by combined scRNA-seq and ST analysis of paired patient samples

To fully decipher PCLM, we performed scRNA-seq on paired samples from three patients (P1–P3) (Figure 1A; Table S1). Using resected specimens from LM allowed us to characterize the cellular components and spatial characteristics comprehensively. After strict quality control, the transcriptomes of a total of 47,587 cells were analyzed using scRNA-seq. Of these, 22,942 single cells were captured in PTs and 24,645 single cells were obtained from paired LMs (Table S2). Using unsupervised clustering analysis, we identified ten cell types based on the scRNA-seq dataset: cancer cells, endothelial cells (ECs), mast cells, fibroblasts, stellate cells, plasma cells, B cells, T cells, mononuclear phagocytes (MPs), and neutrophils (Figure 1B). We analyzed marker genes for cell group specificity and then further identified and visualized mutually exclusive genomes (Figure 1C). The proportions of harvested cell subpopulations varied between PTs and LMs, with cancer cells and stromal cells being more abundant in PTs and immune cells occupying higher proportions in LMs (Figure 1D).

Samples of PTs and paired LMs from one patient (P3) were used for ST. This paired sample developed from the deterioration of a precancerous PC lesion and eventually developed LM (Figure 1E). The presence of cancer cells of different malignant stages in PTs helped us to explore the molecular mechanism of malignant progression, while the existence of adjacent liver (AL) in LM gave us a full picture of metastases. A total of 3,717 spots were detected in PTs, and 2,806 spots were detected in LMs. A good correlation between genes and unique molecular identifier count was observed in both PTs and LMs (Figure 1F; Table S3). Consistent with the morphological results, ST successfully identified cancer cells, stromal cells, and immune cells, with the cancer cell population displaying transcriptional heterogeneity at the spatial level (Figures 1G and 1H). Furthermore, we grouped the detected spots for further analysis (Figure 1I).

LMs exhibit an aggressive transcriptional signature and a highly immunosuppressive profile

In our scRNA-seq results, cancer cells were categorized into low, mediate, and high clusters using the copy-number variation (CNV) scores (Figures S1A–S1C). The proportion of high-CNV_cancer cells was higher in LMs than in PTs (Figure S1D). Gene Ontology (GO) analysis showed that the upregulated genes of metastatic cancer cells were enriched in cell adhesion processes, including the cell-substrate junction and focal adhesion

(Figure S1E). This was consistent with a higher cell-adhesion-process score of cancer cells in LMs compared to in PTs (Figure S1F). Notably, the more active cell adhesion processes appeared mainly within the cancer cells in the tumor border of LMs (Figures S1G and S1H). Furthermore, cancer cells with mediate CNV levels had higher signature scores of immune, metabolism, and metastasis, while high- and low-CNV clusters were more active in stress and inflammation, respectively. Malignant cells in LMs were more active in each biological process except inflammation (Figure S1I). We also found that immune checkpoint molecule LGALS3 was highly expressed in cancer cells, indicating the importance of a LGALS3-mediated mechanism in the immune escape of PCLM (Figures S1J and S1K).

Increased lymphocyte infiltration and higher expression levels of immunosuppressive molecules were detected by scRNA-seq in LMs compared with PTs (Figure S2A; Table S2). To understand the role played by lymphocytes, we reclustered and identified clusters at high resolution (Figures S2B and S2C). Overall, 15,285 T lymphocytes were divided into 15 clusters. We identified CD4 $^{+}$ T cells as four initial clusters, T follicular helper (Tfh)_CD200 cells, and regulatory T (Treg)_FOXP3 cells. Among immune cells, Tfh_CD200 cells and Treg_FOXP3 cells mostly expressed higher levels of immunosuppressive molecules, including CTLA4, CLEC2D, and TIGIT (Figure S2D). They also exhibited high expression levels of T cell co-stimulation and checkpoint molecules (Figure S2E). GO analysis demonstrated that in LMs, Tfh_CD200 cells possessed a more active biological process, including regulation of protein-containing complex assembly and T cell activation (Figure S2F). Treg_FOXP3 cells were more active in regulating leukocyte/lymphocyte activation and mediated immunity (Figure S2G). Tfh_CD200 cells and Treg_FOXP3 cells were found at the end of the putative developmental trajectory (Figure S2H), and the proportions of both were greater in LMs (Figure S2C), indicating a more highly immunosuppressive level in LMs. Among all CD8 $^{+}$ T cell clusters, CD8 T effector memory (CD8Tem)_GZMK (granzyme K) cells possessed higher cytolytic activity, while CD8 T exhausted (CD8Tex)_CXCL13 cells exhibited higher T cell exhaustion levels (Figure S2E). The natural killer (NK) cell cluster consisted of NK_FCGR3A, NK_IFNG, NK_KLRC1, and NK_XCL1, which possessed high cytolytic activity and inflammation-promoting levels (Figure S2E). Moreover, the higher proportion of NK_KLRC1 cells within LMs than in PTs suggests that NK cell cytotoxicity may have been substantially impaired (Figure S2C).¹⁵ We also analyzed the developmental trajectories of CD8 $^{+}$ T cells, NK cells, and B cells (Figure S2H).

PCLM is characterized by increased neutrophil count in the pancreas, blood, and liver

In the cohort comprising 119 patients with PC from Peking Union Medical College Hospital (PUMCH), we have observed that patients with PCLM exhibit elevated levels of CA199, CA125, and CEA compared with those without PCLM. Although no difference was seen in the total white blood cell count, the absolute neutrophil count and neutrophil-to-lymphocyte ratio were significantly increased in patients with PCLM (Figure 2A; Table S4). We used *Kras*^{G12D/+}/*Trp53*^{R172H/+}/*Pdx-1-Cre* (KPC) mice to simulate

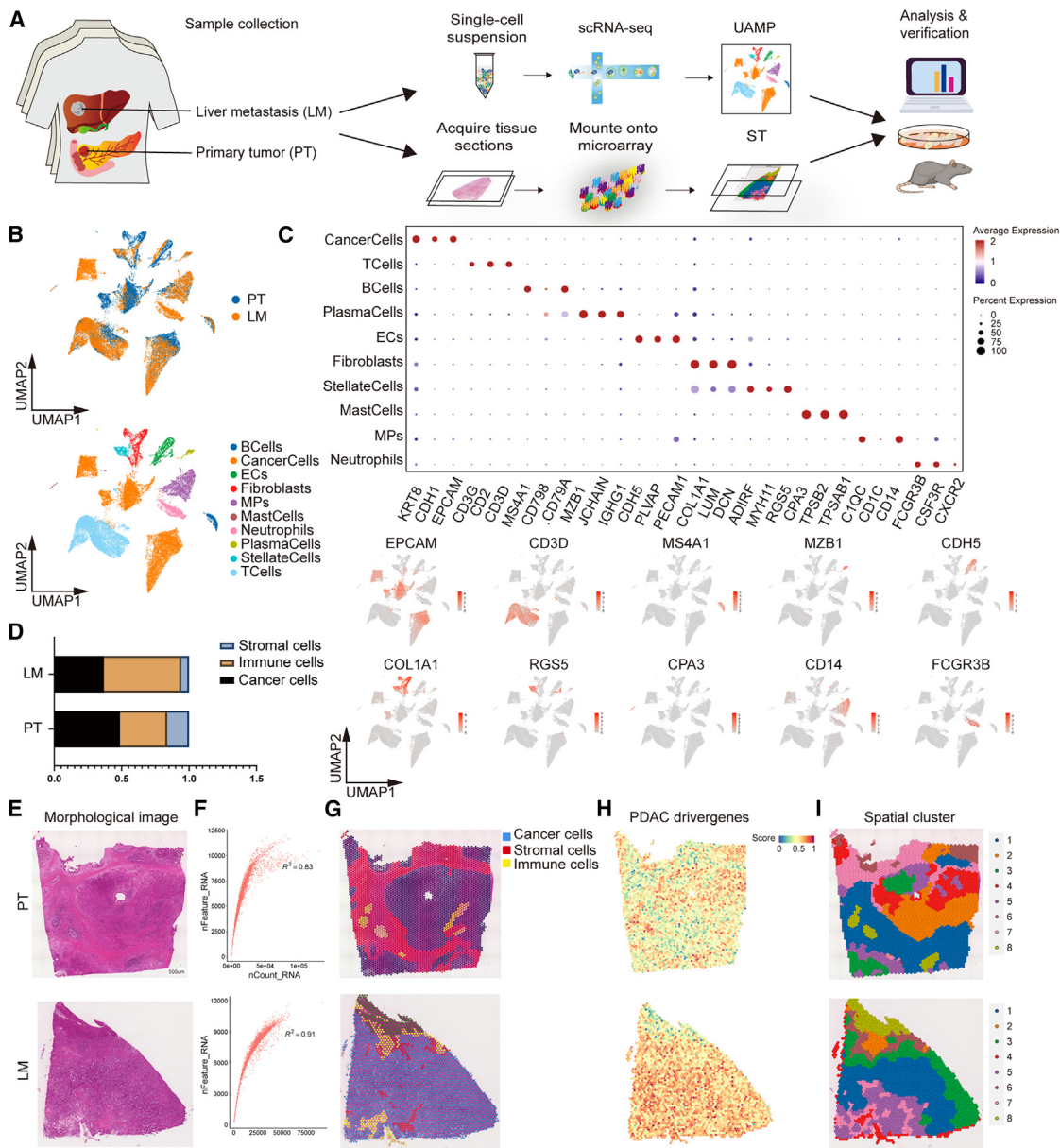


Figure 1. Exploring the PCLM landscape by combined scRNA-seq and ST analysis of paired patient samples

- (A) Schematic overview of scRNA-seq and ST workflow for patients with PCLM ($n = 3$).
- (B) Uniform manifold approximation and projection (UMAP) of major cell types identified based on scRNA-seq dataset.
- (C) Mutually exclusive genomes of 10 major cell types identified by scRNA-seq.
- (D) Proportions of stromal cells, immune cells, and cancer cells captured by scRNA-seq.
- (E) Morphological H&E images of PT and LM samples used for ST. Scale bars: 500 μ m.
- (F) R^2 reflecting the correlation between the number of genes and unique molecular identifier (UMI) count detected by ST.
- (G) Distribution of main cell types of spots in ST identified by H&E staining.
- (H) Visualization of the PDAC driver genes in ST.
- (I) Visualization of spots of different clusters in ST.

See also Figures S1 and S2 and Tables S1–S3.

the biological process of PCLM (Figure 2B) and monitored if KPC mice developed PCLM by 7T magnetic resonance imaging (Figure 2C). Compared with KPC mice without PCLM, those with PCLM exhibited altered proportions of various immune cell types

in the pancreas, blood, and liver by flow cytometry (Figures 2D and S3A). Notably, there was a significant increase in the neutrophil count and proportion across all three tissues (Figures 2E and 2F). Additionally, when PCLM occurred in KPC mice, the

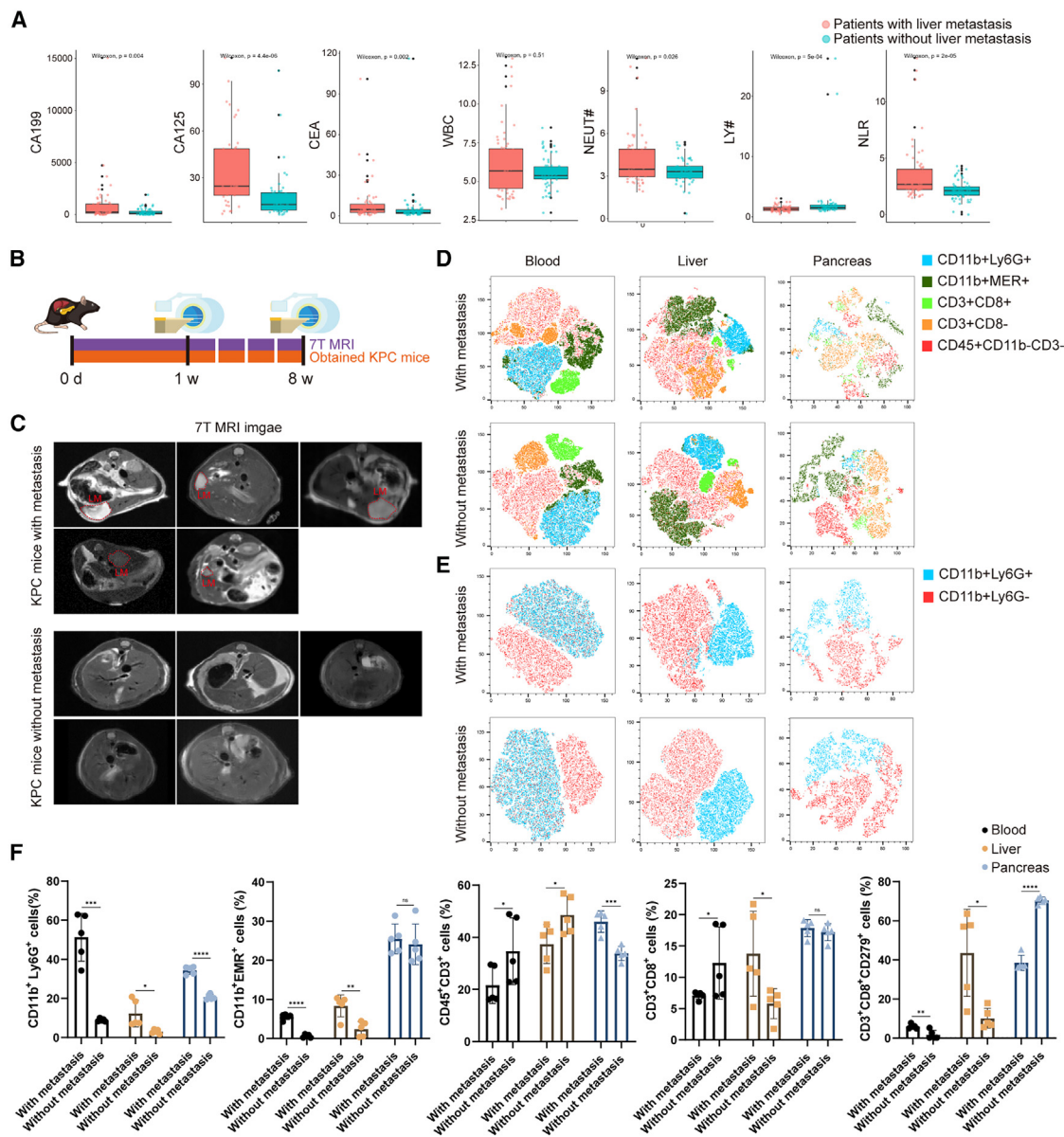


Figure 2. PCLM is characterized by increased neutrophil count in the pancreas, blood, and liver

(A) Quantification of hematological indicators of patients with ($n = 62$) and without ($n = 57$) liver metastasis. The p value was calculated by the Wilcoxon rank-sum test.

(B) Schematic overview of liver metastasis monitoring in KPC mice by 7T MRI.

(C) Representative 7T MRI images of KPC mice livers with ($n = 5$)/without ($n = 5$) liver metastasis. The red dashed lines indicated liver metastases.

(D and E) t-Distributed stochastic neighbor embedding (t-SNE) of CD45⁺ immune cell clusters (D) and CD11b⁺ immune cell clusters (E) in blood, liver, and pancreas of KPC mice with/without liver metastasis measured by flow cytometry.

(F) Proportions of CD11b⁺Ly6G⁺ cells, CD11b⁺MER⁺ cells, CD45⁺CD3⁺ cells, CD3⁺CD8⁺ cells, and CD3⁺CD8⁺CD279⁺ cells in the blood, liver, and pancreas of KPC mice with/without liver metastasis measured by flow cytometry. The p value was calculated by a Student's t test.

Data are presented as the mean \pm SEM.

See also Figure S3 and Table S4.

macrophage proportion was elevated in the blood and liver, with no significant difference observed in the pancreas. The proportion of CD3⁺ T cells decreased in the liver and blood but increased in the pancreas. In the liver, both the proportion of CD8⁺ T cells among total T cells and the expression levels of CD279 on CD8⁺ T cells were high (Figures 2D and 2F).

Neutrophil heterogeneity in PCLM

Neutrophils possess an intrinsic flexibility to adapt to environmental signals regardless of their initial maturation stage.¹³ The scRNA-seq analysis captured more neutrophils in LMs compared with in PTs (Figures 3A and 3B), a finding that was also confirmed at the protein level by immunohistochemistry

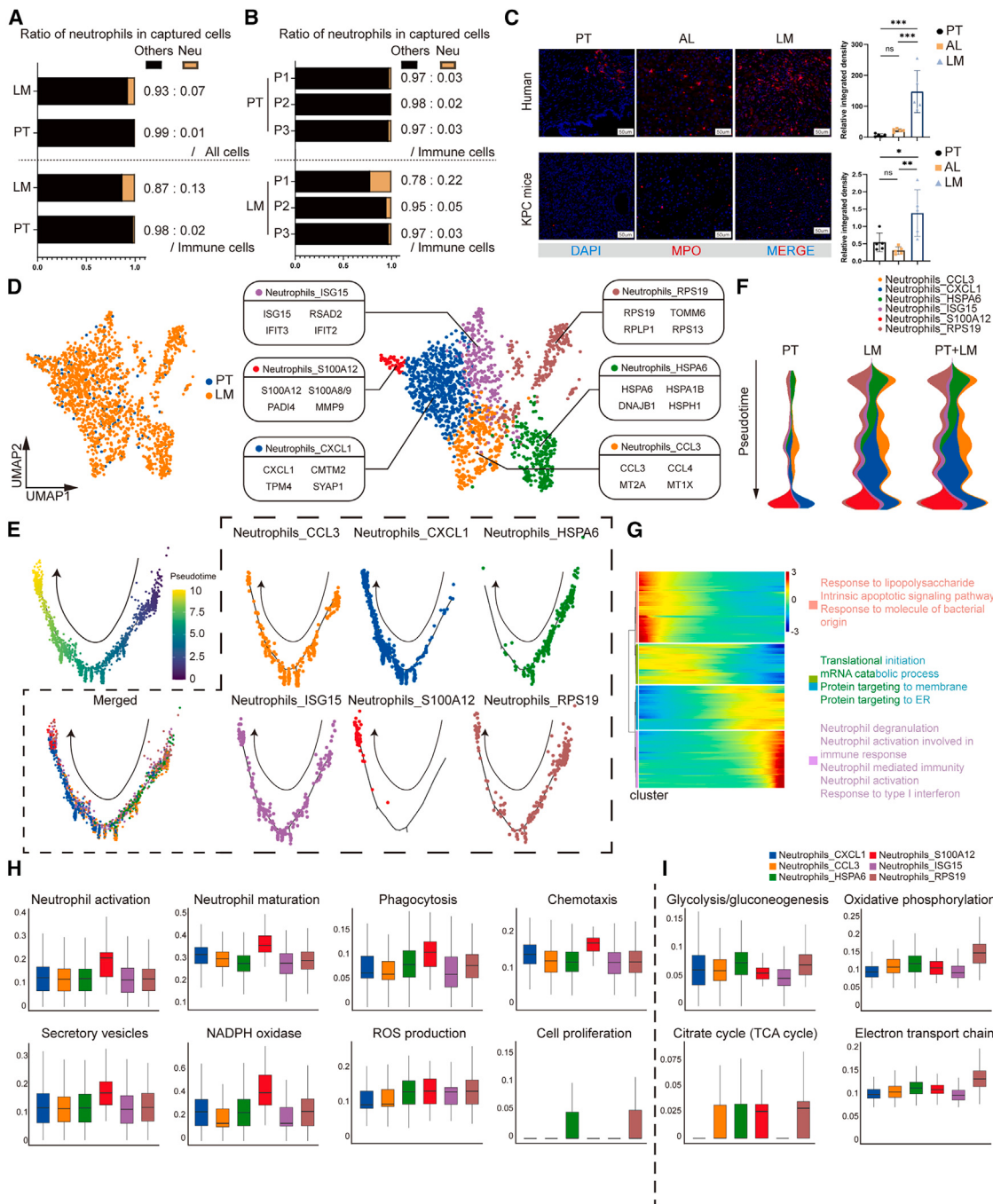


Figure 3. Neutrophil heterogeneity in PCLM

(A) Ratio of neutrophils to all cells (top) and to immune cells (bottom) analyzed by scRNA-seq.

(B) Ratio of neutrophils to immune cells in PT (top) and LM (bottom) samples from P1–P3 analyzed by scRNA-seq.

(C) Representative multiplex immunohistochemistry (mIHC) images (right) and quantitative analyses of relative integrated density of neutrophil in PTs, AL, and LMs (left) of patient (top) and KPC mice (bottom) samples. Scale bars: 50 μm. The *p* value was calculated by one-way ANOVA.

(D) UMAP of neutrophils identified based on scRNA-seq dataset.

(E) Trajectory of neutrophils along pseudotime in a two-dimensional space inferred by Monocle2. Each point corresponds to a single cell.

(F) Group density stream along pseudotime inferred by Monocle2.

(legend continued on next page)

(IHC) assay (Figure 3C). Subsequent characterization identified six distinct neutrophil clusters in our scRNA-seq dataset (Figure 3D; Table S5). Neutrophils_CXCL1 cells did not express obvious functional characteristic genes, and many of their marker genes were also highly expressed in other clusters. Neutrophils_CCL3 cells expressed various chemokines, such as CCL3, CCL4, and CCL3L1. CCL3⁺ neutrophils have been reported to be associated with a low response to tumor immunotherapy.¹⁶ We have identified a class of neutrophils (neutrophils_HSPA6) characterized by unique expression of stress-related heat shock proteins, such as HSPA6 and HSPA1B. The specific expression signature may reflect the stress state of neutrophils_HSPA6 cells, which has been reported to promote metastasis and enhance immunotherapy resistance.¹⁷ Neutrophils_RPS19 cells displayed high expression levels of ribosome-associated proteins RPS19, RPLP1, and RPS13. Neutrophils_ISG15 cells demonstrated high interferon (IFN) response signature. Neutrophils_S100A12 cells highly expressed S100A12, S100A8/9, matrix metalloproteinase 9 (MMP9), and PADI4. Previous studies showed that neutrophils can release S100A protein family molecules, which promotes local inflammation and facilitates tumor cell infiltration.^{18–20} The released MMP9 is involved in remodeling the TME.²¹ As an important mechanism by which neutrophils participate in tumor metastasis, NETs can interact with various components of the TME and promote tumor cell invasion and colonization. NET formation is mainly driven by PADI4; targeting PADI4 has been demonstrated to effectively prevent the NET-mediated functions of neutrophils.^{22,23}

We used Monocle2 to construct the pseudotime map of neutrophils. The initial position on the developmental trajectory was dominated by neutrophils_HSPA6 and neutrophils_RPS19 cells, followed by a concentration of neutrophils_CCL3 and neutrophils_ISG15 cells at the intermediate point of the trajectory. Neutrophils_CXCL1 cells were continuously concentrated in the latter half of the trajectory, while neutrophils_S100A12 cells appeared only at the tail end of the trajectory (Figure 3E). The developmental trajectories of neutrophils in PTs and LMs are highly consistent, indicating that infiltrating neutrophils undergo a similar functional transition process in both types of tumors (Figure 3F). The RNA velocity results demonstrated that early immature neutrophils were mainly active in responding to various extracellular signals and actively regulating the apoptotic state. After continuous and varied stimulation by signals within the TME, neutrophils progressively underwent intracellular biomolecule remodeling. In the final stage, neutrophils were mature and activated and participated in immune responses in diverse ways (Figure 3G).

Furthermore, we performed maturation and function evaluations of each neutrophil cluster in the scRNA-seq dataset. Neutrophils_S100A12 cells had the highest maturation and immune response capabilities, including activation, phagocyt-

tosis, chemotaxis, secretory vesicles, and NADPH oxidase. Neutrophils_HSPA6 and neutrophils_RPS19 cells displayed low levels of maturation and upregulated genes related to cell proliferation (Figure 3H). Our results also showed that six clusters exhibited differences in the activity of metabolic pathways (Figure 3I).

The invasive zone of LM is enriched with pro-metastatic neutrophils_S100A12 cells

Neutrophil_S100A12 cells exhibit gene expression profiles akin to the “N2” phenotype, whereas neutrophils_CCL3 and neutrophils_ISG15 cells lean toward the “N1” characteristics (Figure 4A). To confirm the clinical relevance of neutrophils_S100A12 cells, we retrieved RNA-seq and clinical data from TCGA-PAAD, GEO: GSE224564,²⁴ and ICGC-PAAD cohorts. The results demonstrated that the neutrophils_S100A12 signature was an unfavorable prognostic factor in patients with PC (Figure 4B). To further investigate the role of neutrophils_S100A12 cells, we quantified the expression of characteristic molecules in PCLM samples. We found that S100A12⁺, S100A8/9⁺, PADI4⁺, and MMP9⁺ neutrophils were obviously enriched in LMs (Figure S4A). These data were intriguing because they suggested that neutrophils_S100A12 cells may play a critical role in LM.

The invasive zone is a local spatial area at the tumor border with distinct immunological characteristics, which has been reported in primary liver cancer and some metastatic tumors.^{25,26} This zone is characterized by active inflammatory responses, heightened invasiveness of tumor cells, and substantial infiltration of immune cells, many of which are in a state of compromised immune function.^{27–29} Our ST findings identified the region occupied by cluster 6 as the invasive zone at the front of LM, positioned between cancer cells (cluster 3) and hepatocytes (cluster 8) (Figure 4C). Previous analyses have revealed that cancer cells at the metastatic tumor margin are characterized by the active expression of cell adhesion-related molecules. Multimodal intersection analysis (MIA) revealed that cluster 6 shared a strong similarity to neutrophils_S100A12 cells (Figure 4D). We confirmed the presence of neutrophils_S100A12 cells in this area using H&E staining and IHC assay (Figures 4E, 4F, and S4B). Consistently, key neutrophil pro-metastatic molecules, such as S100A12, S100A8/9, PADI4, and MMP9, also displayed strong positive IHC staining at the invasive zone (Figure S4C). Further analysis revealed a higher positive rate of Ly6G and S100A12 staining in the tumor border than in the tumor center (Figures 4G and 4H). In addition, we did not observe similar enrichment characteristics in other neutrophil clusters (Figure S4D).

NFE2 promotes NET generation by transcriptionally regulating PADI4

Given the diverse array of gene expression profiles in neutrophils, which are typically regulated by transcription factors in

(G) Dynamic changes of gene expression of neutrophils along pseudotime inferred by RNA velocity analysis. The differentially expressed genes were clustered hierarchically into four groups, and the representative enriched pathways of each group are shown.

(H and I) Expression of hallmark signature of selected biological processes (H) and metabolic pathways (I) in each neutrophil cluster measured by Ucell. Data are presented as the mean \pm SEM.

See also Table S5.

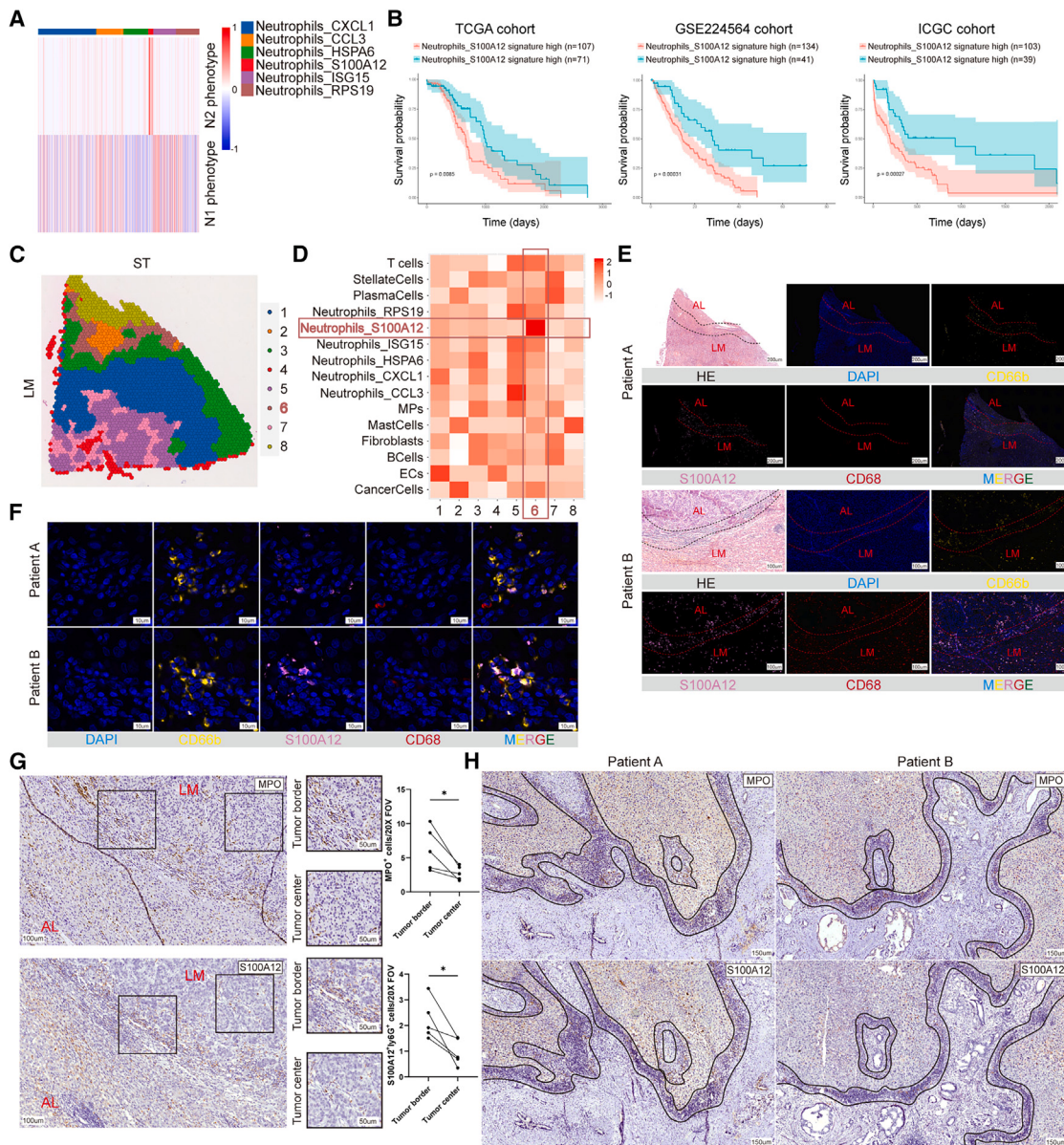


Figure 4. The invasive zone of LM is enriched with pro-metastatic neutrophils_S100A12 cells

(A) Expression of hallmark signature of N1 and N2 phenotypes in each neutrophil cluster.

(B) Kaplan-Meier survival curve presenting the overall survival of patients with PC from TCGA-PAAD (left), GEO: GSE224564 (middle), and ICGC-PAAD (right) cohorts. The patients were divided into two groups according to the expression of the neutrophils_S100A12 signature. The best cutoff was decided by receiver operating characteristic (ROC) curve analysis. The p value was calculated by a log rank test.

(C) Visualization of spots of different clusters in ST of LM. Cluster 6 is highlighted in brown font.

(D) Similarity between clusters identified by ST and cell types identified by scRNA-seq determined by MIA. The strong similarity between cluster 6 and neutrophils_S100A12 cells is framed in brown squares.

(E and F) Representative H&E and mIHC images (DAPI, CD66b, S100A12, CD68, MERGE) of two patient LM samples. Scale bars: 200 μm (E, top), 100 μm (E, bottom), and 10 μm (F).

(G) Representative IHC image and quantitative analyses of myeloperoxidase (MPO) (top) and S100A12 (bottom) cells in the metastatic tumor border ($n = 5$) and tumor center ($n = 5$). Scale bars: 100 μm (left) and 50 μm (right). The p value was calculated by a Student's t test.

(H) Representative IHC image of MPO and S100A12 cells in two patient LM samples. Scale bars: 150 μm. Black dashed lines indicate the invasive zone. Data are presented as the mean ± SEM.

See also Figure S4.

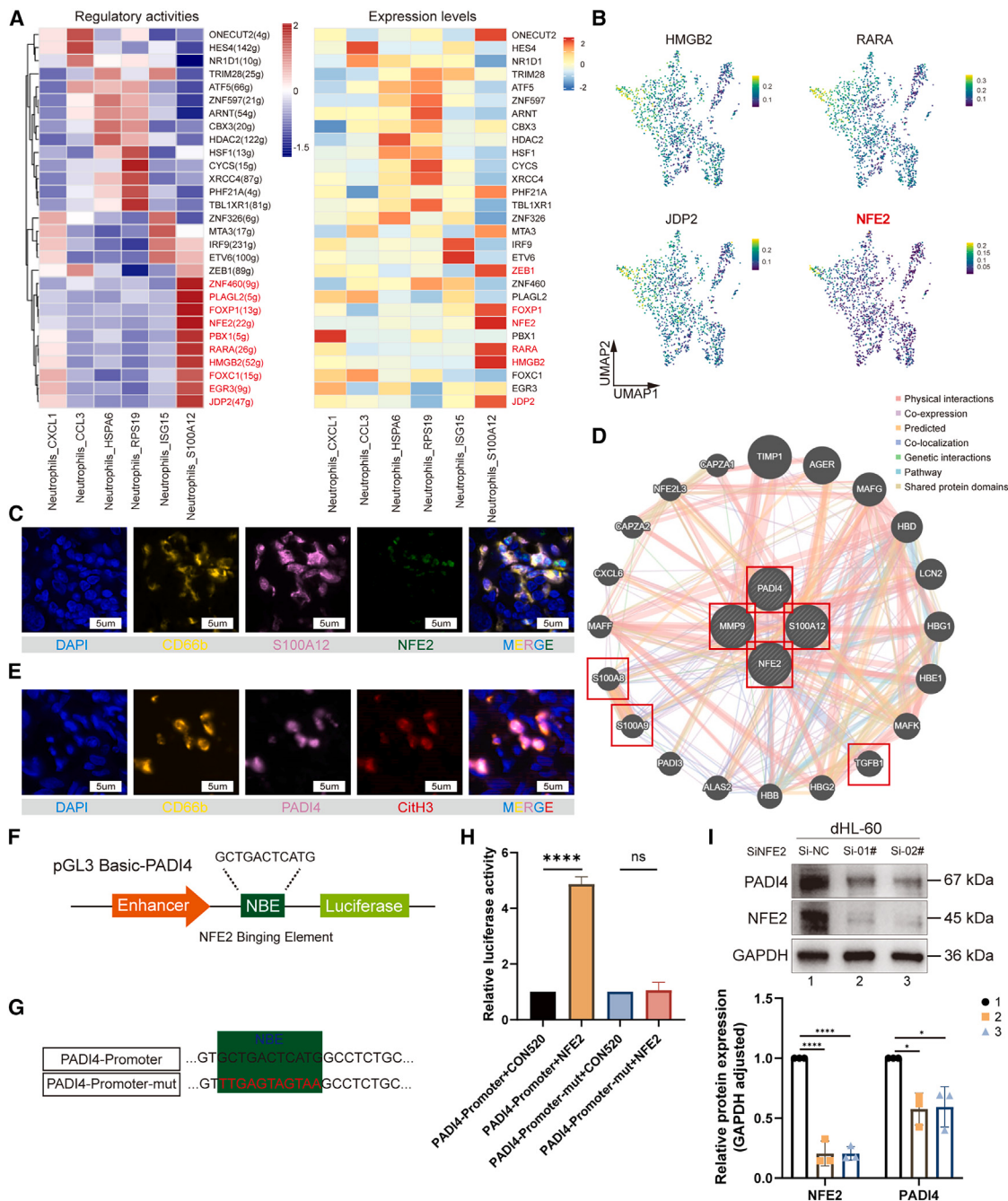


Figure 5. NFE2 promotes NET generation by transcriptionally regulating PADI4

- (A) Transcriptional activities (left) and expression levels (right) of different transcription factors in each neutrophil cluster inferred by pySCENIC.
- (B) UMAP of transcription factors HMGB2, RARA, JDP2, and NFE2 in neutrophils.
- (C) Representative mIHC images (DAPI, CD66b, S100A12, NFE2, MERGE) of LM sample. Scale bars: 5 μ m.
- (D) Prediction of the crosstalk among NFE2 and neutrophils_S100A12 signature genes (S100A12, S100A8/9, PADI4, MMP9) determined by GeneMANIA. NFE2, S100A12, S100A8/9, PADI4, MMP9, and TGFB1 are framed in red squares.
- (E) Representative mIHC images (DAPI, CD66b, PADI4, CitH3, MERGE) of LM sample. Scale bars: 5 μ m.
- (F) Schematic of the NFE2 binding element (NBE) location in the PADI4 promoter sequence of pGL3 basic plasmid.
- (G) Schematic of the wild-type and mutant NBE sequences in the luciferase reporter constructs. The red font indicates mutations in the NBE sequence.
- (H) Relative luciferase activity of different plasmid co-transfection combinations measured by luciferase reporter assay. These assays were conducted in HEK293 cells. The *p* value was calculated by a Student's *t* test.

(legend continued on next page)

response to external stimuli,^{14,30} we analyzed and compared the expression and regulatory activities of different transcription factors in each cluster in the scRNA-seq dataset. The activity and expression levels of HMGB2, RARA, JDP2, and NFE2 were all elevated in neutrophils_S100A12 cells (Figure 5A). Among them, NFE2 exhibited robust cluster specificity and was shown to spatially co-localize with the neutrophils_S100A12 cells (Figures 5B and 5C). In addition, we also observed substantial connections between NFE2 and the characteristic genes of neutrophils_S100A12 cells (Figure 5D).

The NFE2 protein forms a heterodimer that binds to small MAF proteins, forming a complex that binds to regulatory elements as part of a complex regulatory network.³¹ We next questioned how NFE2 can regulate the neutrophil phenotypic conversion. The terminally differentiated pro-metastatic neutrophils_S100A12 cells highly express PADI4 and generate NETs at the invasive front (Figures 5E and S4C). Database analysis suggested that NFE2 could regulate PADI4 expression at the transcriptional level (Table S6). Next, we performed dual-luciferase reporter assays to verify this finding. We constructed luciferase plasmids with wild-type and mutant versions of the *PDAI4* promoter (Figures 5F and 5G). NFE2 pronouncedly increased luciferase activity driven by the wild-type *PDAI4* promoter construct but not the mutant construct (Figure 5H). We further found that small interfering RNA (siRNA)-mediated downregulation of NFE2 expression resulted in reduced expression of PADI4 in differentiated neutrophil-like dHL-60 cells (Figure 5I). These results confirmed that NFE2 directly regulates PADI4 expression via transcriptional regulation of promoter activity.

TGF- β /SMAD3 signaling initiates NFE2-driven neutrophil polarization

The regulatory network involved by NFE2 is closely related to TGF- β signaling (Figure 5D); thus, we hypothesized that metastases-derived TGF- β activates NFE2-driven polarization. The scRNA-seq results revealed that a locally TGF- β -enriched TME was formed in LMs (Figures 6A–6C). We constructed the mouse models and detected higher TGF- β levels in the LM compared with the normal tissue from the same liver region (Figures 6D and 6E). In the same KPC mouse, among the four equal-weight tissues (adjacent pancreas [AP], PTs, AL, and LMs), the concentration of TGF- β is the highest in LMs (Figure 6F).

We simulated the biological process of neutrophil phenotypic polarization following the protocol described by Fridlender et al.³² dHL-60 cells treated with SM16 exhibited lower expression levels of NFE2, and consistent alterations were observed in PADI4 expression (Figure 6G). To confirm that this effect was dependent on TGF- β signaling, we used recombinant TGF- β . The result revealed higher NFE2 levels, accompanied by the upregulation of PADI4 expression, upon stimulation of TGF- β ; in contrast, dHL-60 cells pretreated with the TGF- β receptor (TGF- β R) inhibitor SB431542 failed to exhibit altered NFE2 and PADI4 expression after TGF- β stimulation (Figure 6H).

Similarly, TGF- β stimulation failed to activate the expression of PADI4 in dHL-60 cells after the knockdown of NFE2 (Figure 6I). We next used tumor tissue supernatant (TTS) to stimulate mouse neutrophils. TTS activated the expression of NFE2 and PADI4, whereas boiled TTS lost this ability. Moreover, TTS did not exert these effects in mouse neutrophils after siRNA-mediated down-regulation of NFE2 expression or pretreatment with SB431542 (Figures 6J and S5). In addition, the results suggest that TGF- β neither enhances mouse neutrophil migration nor acts as a chemotactic molecule for mouse neutrophils (Figure S6).

Database prediction analysis suggested that SMAD3, a transcription factor in the canonical TGF- β signaling pathway, regulates the expression of NFE2 (Table S6), indicating that TGF- β -induced NFE2 elevation may also occur at the transcriptional level. We found that SMAD3 modulated NFE2 promoter activity to increase NFE2 protein expression but did not regulate PADI4 promoter activity (Figures 6K and 6L). These results indicate that the activation of NFE2-driven neutrophil phenotypic polarization is dependent on the canonical TGF- β /SMAD3 signaling.

Targeting NFE2-driven neutrophil polarization effectively inhibits PCLM

We next explored the possibility of modulating neutrophil phenotypic polarization to inhibit PCLM. We first evaluated the ability of targeting NFE2-driven neutrophil polarization to modulate the biological behavior of the MIA PaCa-2 cells *in vitro*. After indirect co-culture with TGF- β -activated dHL-60 cells, the MIA PaCa-2 cells showed enhanced viability and invasion ability compared with the control cells, while the promotion ability was weakened after SB43152 pretreatment of dHL-60 cells. siRNA-mediated downregulation of NFE2 expression in dHL-60 cells also abolished the pro-metastatic effect (Figures 7A and 7B). Furthermore, we administered a continuous, low-dose intraperitoneal injection of SM16 into mice that had developed LMs (Figure S7A) and found that the treated tumor-bearing mice showed improved survival and attenuated metastatic burden (Figures S7B–S7E). Livers of SM16-treated mice exhibited lower levels of neutrophil infiltration and reduced proportions of NFE2⁺ and PADI4⁺ neutrophils (Figures S7E and S7F). *Tgfb1*-knockdown Panc02 cells were utilized to establish the mouse model (Figures S7G and S7H), and similar results were observed (Figures S7I–S7L).

Furthermore, we employed anti-mouse Ly6G, cholesterol-modified NFE2 siRNA, and NET inhibitor Cl-amidine to verify the anti-tumor effects of *in vivo* NFE2 interference and its mechanisms. Compared to the negative control group (IgG+SiNC), both neutrophil depletion and SiNFE2 reduced the metastatic burden, with the SiNFE2 group exhibiting an even lower metastatic load. However, the combined application of both did not further enhance the anti-metastatic effect. Additionally, compared to the Cl-amidine group, the SiNFE2 group had a lower metastatic burden (Figures 7C–7E). We co-cultured

(I) dHL-60 cells were transfected with EGFP and NFE2 siRNA (target 1 and target 2). Immunoblots of PADI4, NFE2, and GAPDH are shown. Expression levels of related proteins (GAPDH adjusted) were measured by ImageJ. The p value was calculated by one-way ANOVA.

Data are presented as the mean \pm SEM.

See also Table S6.

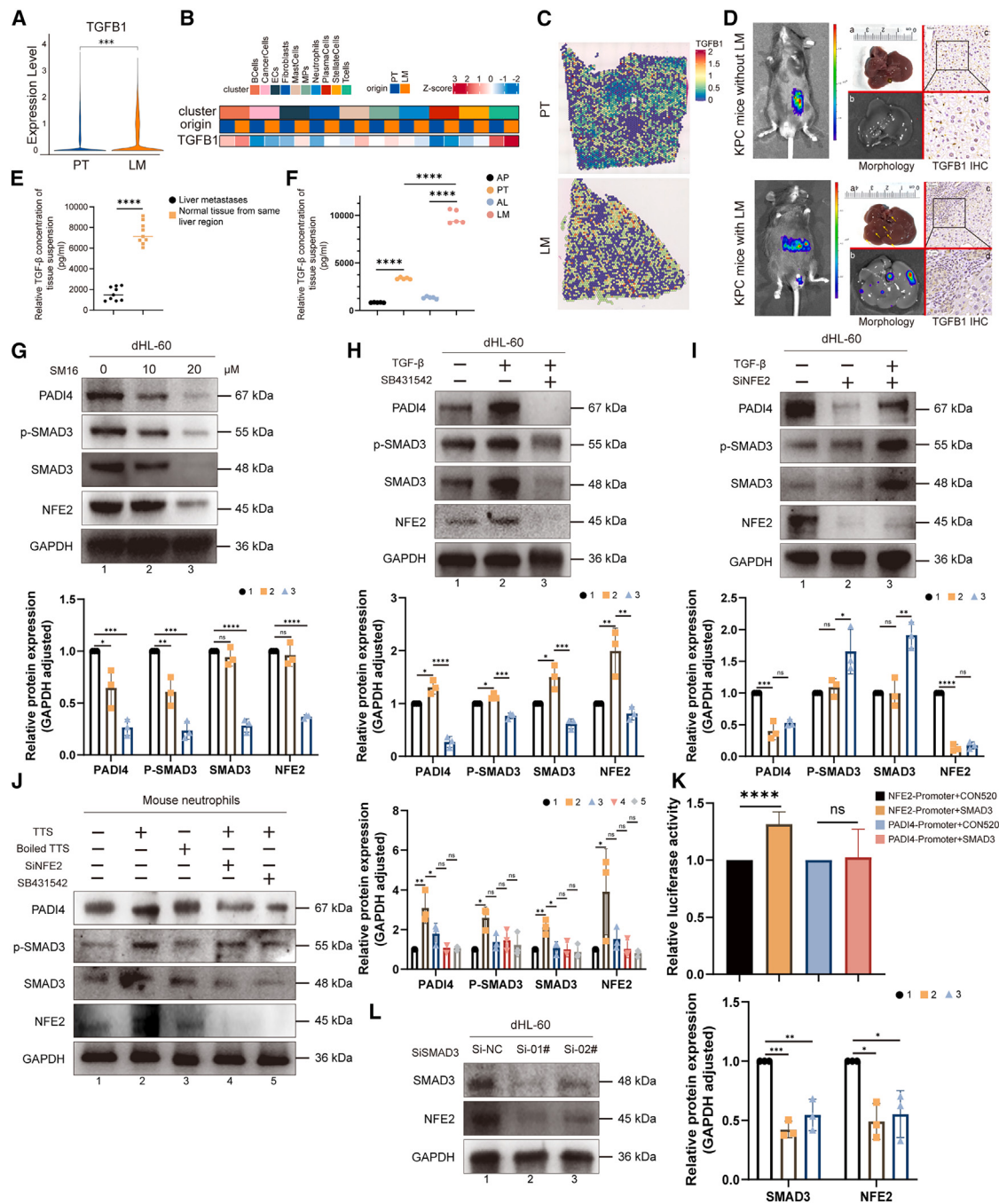


Figure 6. TGF- β /SMAD3 signaling initiates NFE2-driven neutrophil polarization

(A) Expression level of TGFB1 in PTs and LMs identified by scRNA-seq. The p value was calculated by a Wilcoxon rank-sum test.

(B) Expression level of TGFB1 identified by scRNA-seq. Top: cell cluster. Middle: origin. Bottom: relative intensity.

(C) Visualization of the TGFB1 in ST.

(D) Expression of TGF- β of liver of KPC mice with/without LM. Left: *in vivo* bioluminescence images. (a) Morphology. (b) *Ex vivo* bioluminescence images. (c and d) IHC image of TGFB1. Scale bars: 50 μ m (c) and 5 μ m (d).

(E) Relative TGF- β concentration (pg/mL) of tissue suspension from LM ($n = 9$) or normal tissue from the same liver region ($n = 9$) measured by ELISA. The p value was calculated by a Student's t test.

(F) Relative TGF- β concentration (pg/mL) of tissue suspension from KPC mice ($n = 5$) measured by ELISA. AP, adjacent pancreas; PT, primary tumor; AL, adjacent liver; LM, liver metastases. The p value was calculated by a Student's t test.

(legend continued on next page)

neutrophils isolated from the liver of PCLM mice treated with SM16 or SiNFE2 with Panc02 cells and found that *in vivo* treatment inhibited the pro-metastatic capability of neutrophils (Figures 7F–7I).

DISCUSSION

The current anti-metastatic strategies have focused on the PT characteristics rather than the unique features of metastases.^{33,34} The development of PCLM is accompanied by systemic elevated neutrophil counts, especially in the liver. However, the role of neutrophils in this process has not been explored in depth. In this study, we used paired patient samples to characterize the transcriptional heterogeneity of PCLM and the highly immunosuppressive features of LM at the single-cell level. We identified the N2 neutrophils_S100A12 cells, which highly express genes related to inflammation regulation, tumor stromal component remodeling, and NET generation. Spatial analysis indicated that the neutrophils_S100A12 cells specifically aggregated at the invasive front of LM. Furthermore, we found NFE2 to be a key regulatory factor for neutrophil phenotypic polarization. Upon stimulation with metastatic TME-derived TGF- β , the downstream SMAD3 could activate NFE2. NFE2 then drove the neutrophil phenotypic polarization and promoted NET generation at the invasive front. Our study identified the transcriptional and spatial distribution characteristics of the pro-metastatic neutrophil cluster in PCLM, thereby proposing an NFE2-driven neutrophil phenotypic polarization mechanism that may be crucial for developing neutrophil-based anti-metastatic treatments.

Controlling the direction of phenotypic polarization of immune cells to make them more threatening to malignant cells is an important strategy for immunomodulatory therapy.^{35,36} While N1 and N2 phenotypic neutrophil clusters coexist in LM, relatively little is known about how functional heterogeneity is reprogrammed and whether the transformation can be harnessed for therapeutic purposes. Our data suggest that neutrophils underwent polarization from the N1 to the N2 phenotype after infiltration into the tumor. Previous studies have indicated that the pro-tumorigenic effect of neutrophils is dependent on TGF- β .^{32,37,38} We found that tumors were enriched with large amounts of TGF- β , especially LMs, which provided sufficient prerequisites for neutrophil polarization. TGF- β could activate the functional transition of neutrophils through NFE2-induced mechanisms but did not significantly affect neutrophil migration.

Furthermore, depletion of neutrophils in tumor-bearing mice effectively reduced the metastatic burden, while targeted NETs

achieved only limited results. Interfering with NFE2 in neutrophils effectively inhibited tumor cell migration *in vitro*. Meanwhile, *in vivo* SiNFE2 did not enhance the anti-metastatic effect of neutrophil depletion, indicating that *in vivo* anti-metastatic effects of SiNFE2 may require neutrophils to be present. In addition, we found that the anti-metastatic effect of targeted NFE2-driven neutrophil polarization was superior to directly targeting the NETs, possibly because NFE2 serves a potential broader functional regulatory role within neutrophils.³¹

With the advancement of spatial multi-omics, the influence of immune cell spatial characteristics on tumor biological behavior has been gradually emphasized.^{39,40} Our research found that neutrophils accumulate at the invasive front of LM and undergo functional transition, exhibiting a pro-metastatic phenotype. This discovery suggests that dramatic immune reprogramming occurs in the metastatic tumor border. Tumors achieve immune evasion and ectopic growth by co-adapting with the surrounding immune cells. Therefore, disrupting this local immune balance holds promise for precisely inhibiting metastasis progression.^{29,40} In addition, neutrophils are abundant in the metastatic liver and possess strong chemotactic properties and functional plasticity.¹⁴ These characteristics make the NFE2-driven neutrophil polarization a very promising target for anti-metastatic therapy.

Limitations of the study

Our work has the following limitations. First, we found that PCLM is characterized by an increased neutrophil count in the pancreas, blood, and liver, but the mechanism of the systemic inflammatory response induced by metastasis and the neutrophil chemotaxis in metastasis were not analyzed. Second, due to the limited number of paired PCLM specimens available for collection, more experimental validations were warranted. Third, although well acknowledged as TGF- β signaling pathway inhibitors, SM16 and SB431542 are not entirely satisfactory in terms of pathway specificity. Additionally, as few studies have reported the immune characteristics of the metastatic invasive front and the role of neutrophils within this region, as well as due to the limitation of our work, further large-volume studies are required to substantiate the hypothesis.

RESOURCE AVAILABILITY

Lead contact

Further information and requests for resources and reagents should be directed to and will be fulfilled by the lead contact, Dr. Junchao Guo (pumch_research@163.com).

(G–I) dHL-60 cells were treated with 0/10/20 μ M SM16 (G), TGF- β and TGF- β +SB431542 (H), or SiNFE2 and TGF- β +SiNFE2 (I). Immunoblots of PADI4, P-SMAD3, SMAD3, NFE2, and GAPDH are shown. Expression levels of related proteins (GAPDH adjusted) were measured by ImageJ. The *p* value was calculated by one-way ANOVA.

(J) Mouse neutrophils were treated with tumor tissue supernatant (TTS) from LM, boiled TTS, TTS+SiNFE2, and TTS+SB431542. Immunoblots of PADI4, P-SMAD3, SMAD3, NFE2, and GAPDH are shown. Expression levels of related proteins (GAPDH adjusted) were measured by ImageJ. The *p* value was calculated by one-way ANOVA.

(K) Relative luciferase activity of different plasmid co-transfection combinations measured by luciferase reporter assay. These assays were conducted in HEK293 cells. The *p* value was calculated by a Student's *t* test.

(L) dHL-60 cells transfected with SMAD3 siRNA (target 1 and target 2). Immunoblots of SMAD3 and NFE2 are shown. Expression levels of related proteins (GAPDH adjusted) were measured by ImageJ. The *p* value was calculated by one-way ANOVA.

Data are presented as the mean \pm SEM.

See also Figure S5 and S6 and Table S6.

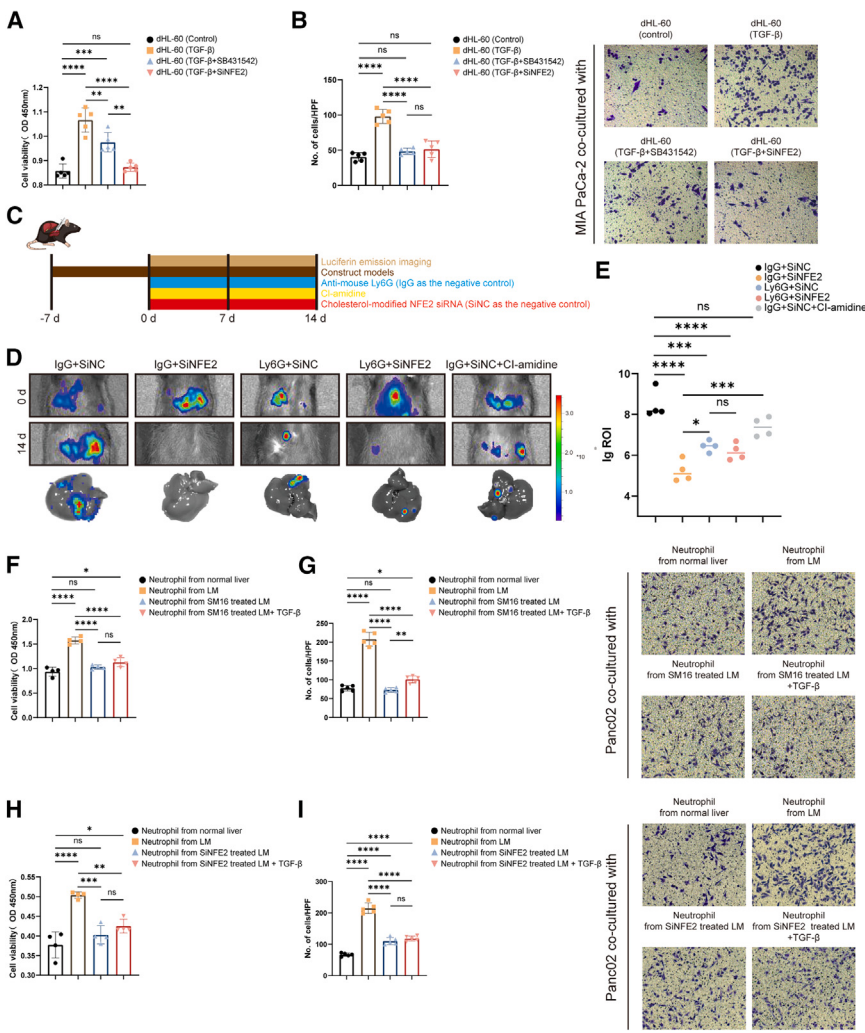


Figure 7. Targeting NFE2-mediated polarization of TANs effectively inhibits PCLM

(A and B) MIA PaCa-2 cells co-cultured with dHL-60 cells that had been pretreated with TGF- β , TGF- β +SB431542, or TGF- β +SiNFE2. Cell viability (optical density [OD] 450 nm) (A) and number of cells/high power field (HPF) (B, left) were measured by CCK-8 test and migration assay. Representative cell migration images are shown (B, right). The *p* value was calculated by one-way ANOVA.

(C) Graphical schematic depicting the procedures of *in vivo* targeted pharmaceutical inhibition assays.

(D and E) Metastases-bearing mice were divided into different treatment groups, including IgG+SINC (*n* = 4), IgG+SiNFE2 (*n* = 4), Ly6G+SINC (*n* = 4), Ly6G+SiNFE2 (*n* = 4), and IgG+SiNFE2+Cl-amidine (*n* = 4). IgG serves as a negative control for Ly6G. SINC serves as a negative control for SiNFE2. Dissolution reagent for Cl-amidine was used as a negative control for Cl-amidine. Representative *in vivo* (top and middle) and *ex vivo* (bottom) bioluminescence images of different groups are shown (D). The relative region of interest (ROI) intensity of the liver regions of different groups were measured by luciferin emission imaging on day 40 (E). The *p* value was calculated by one-way ANOVA.

(F and G) Panc02 cells co-cultured with different pretreated neutrophils, including from normal liver, LM, SM16-treated LM, and SM16-treated LM+*in vitro* TGF- β . Cell viability (OD 450 nm) (F) and number of cells/HPF (G, left) were measured by CCK-8 test and migration assay. Representative cell migration images are shown (G, right). The *p* value was calculated by one-way ANOVA.

(H and I) Panc02 cells co-cultured with different pretreated neutrophils, including from normal liver, LM, SiNFE2-treated LM, and SiNFE2-treated LM+*in vitro* TGF- β . Cell viability (OD 450 nm) (F) and number of cells/HPF (I, left) were measured by CCK-8 test and migration assay. Representative cell migration images are shown (I, right). The *p*-value was calculated by one-way ANOVA.

Data are presented as the mean \pm SEM.

See also Figure S7.

Materials availability

This study did not generate new unique reagents.

Data and code availability

- The processed scRNA-seq and ST data generated in this study have been deposited at GEO and are publicly available as of the date of publication. The accession numbers are listed in the [key resources table](#).
- This paper does not report original code.
- Any additional information required to reanalyze the data reported in this work paper is available from the [lead contact](#) upon request.

ACKNOWLEDGMENTS

This study was supported by the CAMS Innovation Fund for Medical Sciences (CIFMS) (2021-I2M-1-002 and 2022-I2M-C&T-B-030), the Central Government Guides Local Science and Technology Development Fund Projects (236Z2403G), and the National High Level Hospital Clinical Research Funding (2022-PUMCH-D-001). The authors are grateful to CapitalBio Technology for assistance in scRNA-seq data processing. The authors are grateful to Single-ron Bio for assistance in scRNA-seq data analysis. The authors are grateful for the generous gift of cell lines from Dr. Lei You at the Department of General

Surgery of Peking Union Medical College Hospital. The authors are grateful to Theranostics and Translational Research Facility of National Infrastructures for Translational Medicine/Institute of Clinical Medicine/Chinese Academy of Medical Sciences and Peking Union Medical College Hospital for performing 7T magnetic resonance imaging. The authors are grateful to J. Iacona, PhD, from Liwen Bianji (Edanz) (www.liwenbianji.cn) for assistance in editing the English text of a draft of this manuscript.

AUTHOR CONTRIBUTIONS

W.X. and J.L. designed and performed the experiments, analyzed data, and edited the manuscript. Q.L., J.X., and Z.L. assisted with the experiments, analyzed data, and revised the manuscript. L.Z. and H.H. performed the bioinformatic analysis. B.H. collected clinical samples. G.G.X. revised the manuscript. J.G. designed the experiments and supervised manuscript preparation and revision. All authors reviewed or edited the manuscript before submission.

DECLARATION OF INTERESTS

The authors disclose no conflicts of interest.

STAR METHODS

Detailed methods are provided in the online version of this paper and include the following:

- **KEY RESOURCES TABLE**
- **EXPERIMENTAL MODEL AND STUDY PARTICIPANT DETAILS**
 - Human subjects
 - Animal models
 - Cells
- **METHOD DETAILS**
 - 10x single-cell sequencing
 - scRNA-seq data processing, quality control, and data visualization
 - Cell type recognition with Cell-ID
 - Cell malignancy estimation by scCancer
 - Differentially expressed gene (DEG) and pathway enrichment analysis
 - Monocle2
 - RNA velocity
 - Cell-cell interaction (CCI) analysis: CellPhone DB
 - UCell gene set scoring
 - Transcription factor regulatory network analysis: pySCENIC
 - Survival analysis
 - Spatial transcriptomics data processing and clustering
 - Immunohistochemistry (IHC)
 - Intrasplenic injection liver metastasis model
 - Immune cells isolation and flow cytometry
 - *In vitro* pharmaceutical assays
 - Luciferase reporter assay
 - Suspension cell transfection assays
 - Lentiviral infection
 - Western blotting
 - RNA extraction and quantitative real-time PCR
 - ELISA
 - *In vitro* indirect co-culture assays
 - Neutrophil migration assay
- **QUANTIFICATION AND STATISTICAL ANALYSIS**
 - Statistical analysis

SUPPLEMENTAL INFORMATION

Supplemental information can be found online at <https://doi.org/10.1016/j.celrep.2024.115226>.

Received: June 15, 2024

Revised: November 12, 2024

Accepted: December 29, 2024

Published: January 18, 2025

REFERENCES

1. Conroy, T., Desseigne, F., Ychou, M., Bouché, O., Guimbaud, R., Bécouarn, Y., Adenis, A., Raoul, J.L., Gourgou-Bourgade, S., de la Fouchardière, C., et al. (2011). FOLFIRINOX versus gemcitabine for metastatic pancreatic cancer. *N. Engl. J. Med.* 364, 1817–1825. <https://doi.org/10.1056/NEJMoa1011923>.
2. Kim, M.P., Li, X., Deng, J., Zhang, Y., Dai, B., Alton, K.L., Hughes, T.G., Siangco, C., Augustine, J.J., Kang, Y., et al. (2021). Oncogenic KRAS recruits an expansive transcriptional network through mutant p53 to drive pancreatic cancer metastasis. *Cancer Discov.* 11, 2094–2111. <https://doi.org/10.1158/2159-8290.CD-20-1228>.
3. Zhao, Y., Fu, X., Lopez, J.I., Rowan, A., Au, L., Fendler, A., Hazell, S., Xu, H., Horswell, S., Shepherd, S.T.C., et al. (2021). Selection of metastasis competent subclones in the tumour interior. *Nat. Ecol. Evol.* 5, 1033–1045. <https://doi.org/10.1038/s41559-021-01456-6>.
4. Ren, B., Cui, M., Yang, G., Wang, H., Feng, M., You, L., and Zhao, Y. (2018). Tumor microenvironment participates in metastasis of pancreatic cancer. *Mol. Cancer* 17, 108. <https://doi.org/10.1186/s12943-018-0858-1>.
5. Gong, Z., Li, Q., Shi, J., Wei, J., Li, P., Chang, C.H., Shultz, L.D., and Ren, G. (2022). Lung fibroblasts facilitate pre-metastatic niche formation by remodeling the local immune microenvironment. *Immunity* 55, 1483–1500.e9. <https://doi.org/10.1016/j.immuni.2022.07.001>.
6. Liu, Y., and Cao, X. (2016). Characteristics and Significance of the Pre-metastatic Niche. *Cancer Cell* 30, 668–681. <https://doi.org/10.1016/j.ccr.2016.09.011>.
7. Patras, L., Shaashua, L., Matei, I., and Lyden, D. (2023). Immune determinants of the pre-metastatic niche. *Cancer Cell* 41, 546–572. <https://doi.org/10.1016/j.ccr.2023.02.018>.
8. Zou, Y., Ye, F., Kong, Y., Hu, X., Deng, X., Xie, J., Song, C., Ou, X., Wu, S., Wu, L., et al. (2023). The Single-Cell Landscape of Intratumoral Heterogeneity and The Immunosuppressive Microenvironment in Liver and Brain Metastases of Breast Cancer. *Adv. Sci.* 10, e2203699. <https://doi.org/10.1002/advs.202203699>.
9. de Visser, K.E., and Joyce, J.A. (2023). The evolving tumor microenvironment: From cancer initiation to metastatic outgrowth. *Cancer Cell* 41, 374–403. <https://doi.org/10.1016/j.ccr.2023.02.016>.
10. Granot, Z., Henke, E., Comen, E.A., King, T.A., Norton, L., and Benezra, R. (2011). Tumor entrained neutrophils inhibit seeding in the premetastatic lung. *Cancer Cell* 20, 300–314. <https://doi.org/10.1016/j.ccr.2011.08.012>.
11. Liu, Y., Gu, Y., Han, Y., Zhang, Q., Jiang, Z., Zhang, X., Huang, B., Xu, X., Zheng, J., and Cao, X. (2016). Tumor Exosomal RNAs Promote Lung Pre-metastatic Niche Formation by Activating Alveolar Epithelial TLR3 to Recruit Neutrophils. *Cancer Cell* 30, 243–256. <https://doi.org/10.1016/j.ccr.2016.06.021>.
12. Xue, R., Zhang, Q., Cao, Q., Kong, R., Xiang, X., Liu, H., Feng, M., Wang, F., Cheng, J., Li, Z., et al. (2022). Liver tumour immune microenvironment subtypes and neutrophil heterogeneity. *Nature* 612, 141–147. <https://doi.org/10.1038/s41586-022-05400-x>.
13. Ng, M.S.F., Kwok, I., Tan, L., Shi, C., Cerezo-Wallis, D., Tan, Y., Leong, K., Calvo, G.F., Yang, K., Zhang, Y., et al. (2024). Deterministic reprogramming of neutrophils within tumors. *Science* 383, eadf6493. <https://doi.org/10.1126/science.adf6493>.
14. Xiong, S., Dong, L., and Cheng, L. (2021). Neutrophils in cancer carcinogenesis and metastasis. *J. Hematol. Oncol.* 14, 173. <https://doi.org/10.1186/s13045-021-01187-y>.
15. Bexte, T., Alzubi, J., Reindl, L.M., Wendel, P., Schubert, R., Salzmann-Manrique, E., von Metzler, I., Cathomen, T., and Ullrich, E. (2022). CRISPR-Cas9 based gene editing of the immune checkpoint NKG2A enhances NK cell mediated cytotoxicity against multiple myeloma. *Oncolmumonology* 11, 2081415. <https://doi.org/10.1080/2162402x.2022.2081415>.
16. Hu, J., Zhang, L., Xia, H., Yan, Y., Zhu, X., Sun, F., Sun, L., Li, S., Li, D., Wang, J., et al. (2023). Tumor microenvironment remodeling after neoadjuvant immunotherapy in non-small cell lung cancer revealed by single-cell RNA sequencing. *Genome Med.* 15, 14. <https://doi.org/10.1186/s13073-023-01164-9>.
17. Chu, Y., Dai, E., Li, Y., Han, G., Pei, G., Ingram, D.R., Thakkar, K., Qin, J.J., Dang, M., Le, X., et al. (2023). Pan-cancer T cell atlas links a cellular stress response state to immunotherapy resistance. *Nat. Med.* 29, 1550–1562. <https://doi.org/10.1038/s41591-023-02371-y>.
18. Perego, M., Tyurin, V.A., Tyurina, Y.Y., Yellets, J., Nacarelli, T., Lin, C., Nefedova, Y., Kossenkov, A., Liu, Q., Sreedhar, S., et al. (2020). Reactivation of dormant tumor cells by modified lipids derived from stress-activated neutrophils. *Sci. Transl. Med.* 12, eabb5817. <https://doi.org/10.1126/scitranslmed.abb5817>.
19. Zhan, X., Wu, R., Kong, X.H., You, Y., He, K., Sun, X.Y., Huang, Y., Chen, W.X., and Duan, L. (2023). Elevated neutrophil extracellular traps by HBV-mediated S100A9-TLR4/RAGE-ROS cascade facilitate the growth and

- metastasis of hepatocellular carcinoma. *Cancer Commun.* 43, 225–245. <https://doi.org/10.1002/cac2.12388>.
20. Yao, Z., Zhang, B., Niu, G., Yan, Z., Tong, X., Zou, Y., Li, Y., and Yang, M. (2022). Neutrophil Infiltration Characterized by Upregulation of S100A8, S100A9, S100A12 and CXCR2 Is Associated With the Co-Occurrence of Crohn's Disease and Peripheral Artery Disease. *Front. Immunol.* 13, 896645. <https://doi.org/10.3389/fimmu.2022.896645>.
 21. Zhang, Q., Liu, S., Wang, H., Xiao, K., Lu, J., Chen, S., Huang, M., Xie, R., Lin, T., and Chen, X. (2023). ETV4 Mediated Tumor-Associated Neutrophil Infiltration Facilitates Lymphangiogenesis and Lymphatic Metastasis of Bladder Cancer. *Adv. Sci.* 10, e2205613. <https://doi.org/10.1002/advs.202205613>.
 22. Teijeira, Á., Garasa, S., Gato, M., Alfaro, C., Migueliz, I., Cirella, A., de Andrea, C., Ochoa, M.C., Otano, I., Etxeberria, I., et al. (2020). CXCR1 and CXCR2 Chemokine Receptor Agonists Produced by Tumors Induce Neutrophil Extracellular Traps that Interfere with Immune Cytotoxicity. *Immunity* 52, 856–871.e8. <https://doi.org/10.1016/j.immuni.2020.03.001>.
 23. Kajioka, H., Kagawa, S., Ito, A., Yoshimoto, M., Sakamoto, S., Kikuchi, S., Kuroda, S., Yoshida, R., Umeda, Y., Noma, K., et al. (2021). Targeting neutrophil extracellular traps with thrombomodulin prevents pancreatic cancer metastasis. *Cancer Lett.* 497, 1–13. <https://doi.org/10.1016/j.canlet.2020.10.015>.
 24. Ohara, Y., Tang, W., Liu, H., Yang, S., Dorsey, T.H., Cawley, H., Moreno, P., Chari, R., Guest, M.R., Azizian, A., et al. (2023). SERPINB3-MYC axis induces the basal-like/squamous subtype and enhances disease progression in pancreatic cancer. *Cell Rep.* 42, 113434. <https://doi.org/10.1016/j.celrep.2023.113434>.
 25. Wu, L., Yan, J., Bai, Y., Chen, F., Zou, X., Xu, J., Huang, A., Hou, L., Zhong, Y., Jing, Z., et al. (2023). An invasive zone in human liver cancer identified by Stereo-seq promotes hepatocyte-tumor cell crosstalk, local immunosuppression and tumor progression. *Cell Res.* 33, 585–603. <https://doi.org/10.1038/s41422-023-00831-1>.
 26. Rao, D., Li, J., Zhang, M., Huang, S., Meng, L., Song, G., Ma, J., Wu, Y., Cheng, Y., Ji, S., et al. (2024). Multi-model analysis of gallbladder cancer reveals the role of OxLDL-absorbing neutrophils in promoting liver invasion. *Exp. Hematol. Oncol.* 13, 58. <https://doi.org/10.1186/s40164-024-00521-7>.
 27. Cheng, X., Cao, Y., Liu, X., Li, Y., Li, Q., Gao, D., and Yu, Q. (2024). Single-cell and spatial omics unravel the spatiotemporal biology of tumour border invasion and haematogenous metastasis. *Clin. Transl. Med.* 14, e70036. <https://doi.org/10.1002/ctm2.70036>.
 28. Mo, C.K., Liu, J., Chen, S., Storrs, E., Targino da Costa, A.L.N., Houston, A., Wendl, M.C., Jayasinghe, R.G., Iglesia, M.D., Ma, C., et al. (2024). Tumour evolution and microenvironment interactions in 2D and 3D space. *Nature* 634, 1178–1186. <https://doi.org/10.1038/s41586-024-08087-4>.
 29. Ozato, Y., Kojima, Y., Kobayashi, Y., Hisamatsu, Y., Toshima, T., Yonemura, Y., Masuda, T., Kagawa, K., Goto, Y., Utou, M., et al. (2023). Spatial and single-cell transcriptomics decipher the cellular environment containing HLA-G+ cancer cells and SPP1+ macrophages in colorectal cancer. *Cell Rep.* 42, 111929. <https://doi.org/10.1016/j.celrep.2022.111929>.
 30. Jaillon, S., Ponzetta, A., Di Mitri, D., Santoni, A., Bonecchi, R., and Mantovani, A. (2020). Neutrophil diversity and plasticity in tumour progression and therapy. *Nat. Rev. Cancer* 20, 485–503. <https://doi.org/10.1038/s41568-020-0281-y>.
 31. Gasiorek, J.J., and Blank, V. (2015). Regulation and function of the NFE2 transcription factor in hematopoietic and non-hematopoietic cells. *Cell. Mol. Life Sci.* 72, 2323–2335. <https://doi.org/10.1007/s00018-015-1866-6>.
 32. Fridlender, Z.G., Sun, J., Kim, S., Kapoor, V., Cheng, G., Ling, L., Worthen, G.S., and Albelda, S.M. (2009). Polarization of tumor-associated neutrophil phenotype by TGF-beta: "N1" versus "N2" TAN. *Cancer Cell* 16, 183–194. <https://doi.org/10.1016/j.ccr.2009.06.017>.
 33. Yu, J., Green, M.D., Li, S., Sun, Y., Journey, S.N., Choi, J.E., Rizvi, S.M., Qin, A., Waninger, J.J., Lang, X., et al. (2021). Liver metastasis restrains immunotherapy efficacy via macrophage-mediated T cell elimination. *Nat. Med.* 27, 152–164. <https://doi.org/10.1038/s41591-020-1131-x>.
 34. Turajlic, S., and Swanton, C. (2016). Metastasis as an evolutionary process. *Science* 352, 169–175. <https://doi.org/10.1126/science.aaf2784>.
 35. Astuti, Y., Raymant, M., Quaranta, V., Clarke, K., Abudula, M., Smith, O., Bellomo, G., Chandran-Gorner, V., Nourse, C., Halloran, C., et al. (2024). Efferocytosis reprograms the tumor microenvironment to promote pancreatic cancer liver metastasis. *Nat. Can. (Ott.)* 5, 774–790. <https://doi.org/10.1038/s43018-024-00731-2>.
 36. McGinnis, C.S., Miao, Z., Superville, D., Yao, W., Goga, A., Reticker-Flynn, N.E., Winkler, J., and Satpathy, A.T. (2024). The temporal progression of lung immune remodeling during breast cancer metastasis. *Cancer Cell* 42, 1018–1031.e6. <https://doi.org/10.1016/j.ccr.2024.05.004>.
 37. Chung, J.Y.F., Tang, P.C.T., Chan, M.K.K., Xue, V.W., Huang, X.R., Ng, C.S.H., Zhang, D., Leung, K.T., Wong, C.K., Lee, T.L., et al. (2023). Smad3 is essential for polarization of tumor-associated neutrophils in non-small cell lung carcinoma. *Nat. Commun.* 14, 1794. <https://doi.org/10.1038/s41467-023-37515-8>.
 38. Tian, S., Chu, Y., Hu, J., Ding, X., Liu, Z., Fu, D., Yuan, Y., Deng, Y., Wang, G., Wang, L., and Wang, Z. (2022). Tumour-associated neutrophils secrete AGR2 to promote colorectal cancer metastasis via its receptor CD98hc-xCT. *Gut* 71, 2489–2501. <https://doi.org/10.1136/gutjnl-2021-325137>.
 39. Hsieh, W.C., Budiarso, B.R., Wang, Y.F., Lin, C.Y., Gwo, M.C., So, D.K., Tzeng, Y.S., and Chen, S.Y. (2022). Spatial multi-omics analyses of the tumor immune microenvironment. *J. Biomed. Sci.* 29, 96. <https://doi.org/10.1186/s12929-022-00879-y>.
 40. Fu, T., Dai, L.J., Wu, S.Y., Xiao, Y., Ma, D., Jiang, Y.Z., and Shao, Z.M. (2021). Spatial architecture of the immune microenvironment orchestrates tumor immunity and therapeutic response. *J. Hematol. Oncol.* 14, 98. <https://doi.org/10.1186/s13045-021-01103-4>.
 41. Butler, A., Hoffman, P., Smibert, P., Papalexakis, E., and Satija, R. (2018). Integrating single-cell transcriptomic data across different conditions, technologies, and species. *Nat. Biotechnol.* 36, 411–420. <https://doi.org/10.1038/nbt.4096>.
 42. Zhao, E., Stone, M.R., Ren, X., Guenthoer, J., Smythe, K.S., Pulliam, T., Williams, S.R., Uytingco, C.R., Taylor, S.E.B., Nghiem, P., et al. (2021). Spatial transcriptomics at subspot resolution with BayesSpace. *Nat. Biotechnol.* 39, 1375–1384. <https://doi.org/10.1038/s41587-021-00935-2>.
 43. Zheng, G.X.Y., Terry, J.M., Belgrader, P., Ryvkin, P., Bent, Z.W., Wilson, R., Ziraldo, S.B., Wheeler, T.D., McDermott, G.P., Zhu, J., et al. (2017). Massively parallel digital transcriptional profiling of single cells. *Nat. Commun.* 8, 14049. <https://doi.org/10.1038/ncomms14049>.
 44. Wolf, F.A., Angerer, P., and Theis, F.J. (2018). SCANPY: large-scale single-cell gene expression data analysis. *Genome Biol.* 19, 15. <https://doi.org/10.1186/s13059-017-1382-0>.
 45. Patel, A.P., Tirosi, I., Trombetta, J.J., Shalek, A.K., Gillespie, S.M., Wakimoto, H., Cahill, D.P., Nahed, B.V., Curry, W.T., Martuza, R.L., et al. (2014). Single-cell RNA-seq highlights intratumoral heterogeneity in primary glioblastoma. *Science* 344, 1396–1401. <https://doi.org/10.1126/science.1254257>.
 46. Yu, G., Wang, L.G., Han, Y., and He, Q.Y. (2012). clusterProfiler: an R package for comparing biological themes among gene clusters. *OMICS* 16, 284–287. <https://doi.org/10.1089/omi.2011.0118>.
 47. Qiu, X., Hill, A., Packer, J., Lin, D., Ma, Y.A., and Trapnell, C. (2017). Single-cell mRNA quantification and differential analysis with Census. *Nat. Methods* 14, 309–315. <https://doi.org/10.1038/nmeth.4150>.
 48. Bergen, V., Lange, M., Peidli, S., Wolf, F.A., and Theis, F.J. (2020). Generalizing RNA velocity to transient cell states through dynamical modeling. *Nat. Biotechnol.* 38, 1408–1414. <https://doi.org/10.1038/s41587-020-0591-3>.
 49. Efremova, M., Vento-Tormo, M., Teichmann, S.A., and Vento-Tormo, R. (2020). CellPhoneDB: inferring cell-cell communication from combined

- expression of multi-subunit ligand-receptor complexes. *Nat. Protoc.* 15, 1484–1506. <https://doi.org/10.1038/s41596-020-0292-x>.
50. Andreatta, M., and Carmona, S.J. (2021). UCell: Robust and scalable single-cell gene signature scoring. *Comput. Struct. Biotechnol. J.* 19, 3796–3798. <https://doi.org/10.1016/j.csbj.2021.06.043>.
51. Van de Sande, B., Flierin, C., Davie, K., De Waegeneer, M., Hulselmans, G., Aibar, S., Seurinck, R., Saelens, W., Cannoodt, R., Rouchon, Q., et al. (2020). A scalable SCENIC workflow for single-cell gene regulatory network analysis. *Nat. Protoc.* 15, 2247–2276. <https://doi.org/10.1038/s41596-020-0336-2>.
52. Suzuki, E., Kim, S., Cheung, H.K., Corbley, M.J., Zhang, X., Sun, L., Shan, F., Singh, J., Lee, W.C., Albelda, S.M., and Ling, L.E. (2007). A novel small-molecule inhibitor of transforming growth factor beta type I receptor kinase (SM16) inhibits murine mesothelioma tumor growth in vivo and prevents tumor recurrence after surgical resection. *Cancer Res.* 67, 2351–2359. <https://doi.org/10.1158/0008-5472.Can-06-2389>.
53. Fu, K., Corbley, M.J., Sun, L., Friedman, J.E., Shan, F., Papadatos, J.L., Costa, D., Lutterodt, F., Sweigard, H., Bowes, S., et al. (2008). SM16, an orally active TGF-beta type I receptor inhibitor prevents myofibroblast induction and vascular fibrosis in the rat carotid injury model. *Arterioscler. Thromb. Vasc. Biol.* 28, 665–671. <https://doi.org/10.1161/atvaha.107.158030>.
54. Inman, G.J., Nicolás, F.J., Callahan, J.F., Harling, J.D., Gaster, L.M., Reith, A.D., Laping, N.J., and Hill, C.S. (2002). SB-431542 is a potent and specific inhibitor of transforming growth factor-beta superfamily type I activin receptor-like kinase (ALK) receptors ALK4, ALK5, and ALK7. *Mol. Pharmacol.* 62, 65–74. <https://doi.org/10.1124/mol.62.1.65>.

STAR★METHODS

KEY RESOURCES TABLE

REAGENT or RESOURCE	SOURCE	IDENTIFIER
Antibodies		
Goat Anti-Rabbit IgG H&L (HRP)	Abcam	Cat# ab205718; RRID:AB_2819160
Recombinant Anti-S100A12/CGRP antibody	Abcam	Cat# ab272713; RRID:AB_2920851
Recombinant Anti-S100A8 + S100A9 antibody	Abcam	Cat# ab288715
PADI4 antibody	Proteintech	Cat# 17373-1-AP; RRID:AB_2878398
Recombinant Anti-MMP9 antibody	Abcam	Cat# ab283575; RRID:AB_2928971
TGM2 antibody	Proteintech	Cat# 15100-1-AP; RRID:AB_2202885
Galectin-3 Polyclonal antibody	Proteintech	Cat# 14979-1-AP; RRID:AB_2136768
Recombinant Anti-Ly6g antibody	Abcam	Cat# ab238132; RRID:AB_2923218
MPO antibody	Proteintech	Cat# 22225-1-AP; RRID:AB_2879037
Recombinant Anti-CD66b antibody	Abcam	Cat# ab300122; RRID:AB_3097803
Mouse Anti-CD68 Monoclonal Antibody, Unconjugated, Clone KP1	Abcam	Cat# ab955; RRID:AB_307338
NFE2 antibody	Proteintech	Cat# 11089-1-AP; RRID:AB_2152928
Recombinant Anti-Histone H3 (citrulline R2 + R8 + R17) antibody	Abcam	Cat# ab281584
Recombinant Anti-Macrophage Inflammatory Protein 1 alpha/CCL3 + CCL3L1 antibody	Abcam	Cat# ab259372; RRID:AB_3094596
ISG15 antibody	Proteintech	Cat# 15981-1-AP; RRID:AB_2126302
GRO Alpha antibody	Proteintech	Cat# 12335-1-AP; RRID:AB_2087568
HSPA6 antibody	Proteintech	Cat# 13616-1-AP; RRID:AB_2120122
RPS19 antibody	Proteintech	Cat# 15085-1-AP; RRID:AB_2180202
Fixable Viability Stain 780	BD Biosciences	Cat# 565388; RRID:AB_2869673
Purified Rat Anti-Mouse CD16/CD32 (Mouse BD Fc Block™) Clone 2.4G2	BD Biosciences	Cat# 553141; RRID:AB_394656
FITC anti-mouse CD45 Recombinant	BioLegend	Cat# 157608; RRID:AB_2832554
Brilliant Violet 421(TM) anti-mouse/human CD11b	BioLegend	Cat# 101235; RRID:AB_10897942
PE anti-mouse Ly-6G	BioLegend	Cat# 127607; RRID:AB_1186104
Alexa Fluor(R) 700 anti-mouse CD3	BioLegend	Cat# 100216; RRID:AB_493697
Brilliant Violet 510(TM) anti-mouse CD8a	BioLegend	Cat# 100752; RRID:AB_2563057
PerCP/Cyanine5.5 anti-mouse F4/80	BioLegend	Cat# 123128; RRID:AB_893484
PE/Cyanine7 anti-mouse CD279 (PD-1)	BioLegend	Cat# 109110; RRID:AB_572017
HRP-conjugated goat anti-mouse secondary antibody	Zsbio	ZB-2305
HRP-conjugated goat anti-rabbit secondary antibody	Zsbio	ZB-2306
Bacterial and virus strains		
LV-Tgfb1-RNAi	Genechem	N/A
LV-Luciferase	Genechem	N/A
Biological samples		
Surgical excision samples	Peking Union Medical College Hospital	N/A
Chemicals, peptides, and recombinant proteins		
SM16	MedChemExpress	Cat# HY-111482
Cl-amidine	Selleck	Cat# S8141

(Continued on next page)

Continued

REAGENT or RESOURCE	SOURCE	IDENTIFIER
anti-mouse Ly6G	BioXcell	Cat# BE0075-1
IgG2a isotype control	BioXcell	Cat# BE0085
SB431542	MedChemExpress	Cat# HY-10431
HumanKine® recombinant human TGF-β	Proteintech	Cat# HZ-1011
Collagenase IV	Thermo Fisher SCIENTIFIC	Cat# 17104019
DNase I	Thermo Fisher SCIENTIFIC	Cat# 90083
Dispase II	Thermo Fisher SCIENTIFIC	Cat# 17105041
Heparin sodium	MedChemExpress	Cat# HY-17567A
EGTA	Beyotime Biotechnology	Ca# ST068
DMEM/F12	Gibco	Cat# 11320033
DMEM	Gibco	Cat# 11965118
IMDM	Procell	Cat# PM150510
RPMI-1640	Procell	Cat# PM150110
PBS	Procell	Cat# PB180327
FBS	Thermo Fisher SCIENTIFIC	Cat# A3160901
BSA	Beyotime Biotechnology	Cat# ST023
DPBS	Thermo Fisher SCIENTIFIC	Cat# 14190144
Percoll	Cytiva	Cat# 17089101
Penicillin-Streptomycin Solution	Beyotime Biotechnology	Cat# C0222
Puromycin	MedChemExpress	Cat# HY-B1743A
DMSO	Thermo Fisher SCIENTIFIC	Cat# D12345
Lipofectamine 3000 Transfection Reagent	Thermo Fisher SCIENTIFIC	Cat# L3000001
RIPA Lysis Buffer	APPLYGEN	Cat# C1053-100
Protease inhibitor cocktail	Aqlabtech	Cat# AQ551
Phosphatase inhibitor	APPLYGEN	Cat# P1260
PMSF	Beyotime Biotechnology	Cat# ST505
Skim milk	Aqlabtech	Cat# AQ62321
SYBR Green Master Mix	Thermo Fisher SCIENTIFIC	Cat# A25742
Crystal violet	Beyotime Biotechnology	Cat# C0121
Red Blood Cell Lysis Buffer	Beyotime Biotechnology	Cat# C3702
G418	Beyotime Biotechnology	Cat# ST081

Critical commercial assays

Single Cell 3' GEM, Library & Gel Bead Kit V3.1	10x Genomics	N/A
Chromium Single Cell B Chip Kit	10x Genomics	N/A
PANO 7-plex IHC kit	Panovue	Cat# 0004100100
Dual Luciferase Reporter Assay	Promega	Cat# E1910
SF Cell Line 4D-Nucleofector™ X Kit S	Lonza Bioscience	Cat# V4XC-2024
Human Monocyte Nucleofector® Kit	Lonza Bioscience	Cat# VPA-1007
Enhanced BCA Protein Assay Kit	Beyotime Biotechnology	Cat# P0010
Super ECL Reagent	Aqlabtech	Cat# AQ529
RNA-Quick Purification Kit	ESScience	Cat# RN001
PrimeScript RT reagent Kit	Takara	Cat# RR047A
Mouse TGF-beta 1 ELISA Kit	RayBiotech	Cat# P04202
MycoBlue Mycoplasma Detector Kit	Vazyme	Cat# D101
Cell counting kit 8	Dojindo	Cat# CK04-05

Deposited data

scRNA-seq and ST data	This paper	GSE281288
JASPAR database		https://jaspar.genereg.net/
TCGA data		https://xenabrowser.net/

(Continued on next page)

Continued

REAGENT or RESOURCE	SOURCE	IDENTIFIER
ICGC data		https://platform.icgc-argo.org/
GSE224564 data		https://www.ncbi.nlm.nih.gov/geo/query/acc.cgi?acc=GSE224564
Experimental models: Cell lines		
HL-60	Procell	Cat# CL-0110
HEK-293	Procell	Cat# CL-0005
MIA PaCa-2	Procell	Cat# CL-0627
Panc02	N/A	N/A
Experimental models: Organisms/strains		
C57BL/6 mice, male	Cyagen BioTech	N/A
Kras ^{G12D/+} /Trp53 ^{R172H/+} /Pdx-1-Cre (KPC) mice	Cyagen BioTech	N/A
Oligonucleotides		
See Table S7 for sequence information		
Recombinant DNA		
pGL3 Basic-PADI4-WT	Genechem	N/A
pGL3 Basic-PADI4-Mut	Genechem	N/A
pGL3 Basic-SMAD3	Genechem	N/A
pGL3 Basic-Renilla	Genechem	N/A
Software and algorithms		
R package Seurat v4.0.1	(Butler et al.) ⁴¹	N/A
R package BayesSpace v1.2.0	(Zhao et al.) ⁴²	N/A
R package Cellranger v6.1.0	(Zheng et al.) ⁴³	N/A
R package Scanpy v1.8.2	(Wolf et al.) ⁴⁴	N/A
R package InferCNV v1.20.0	(Patel et al.) ⁴⁵	N/A
R package ClusterProfiler v4.12.6	(Yu et al.) ⁴⁶	N/A
R package Monocle2 v2.10.0	(Qiu et al.) ⁴⁷	N/A
R package scVelo v0.17.17	(Bergen et al.) ⁴⁸	N/A
R package Cellphone DB v2.1.0	(Efremova et al.) ⁴⁹	N/A
R package UCell v1.1.0	(Andreatta et al.) ⁵⁰	N/A
R package pycnemic v0.11.0	(Van et al.) ⁵¹	N/A
R version 4.1.0, 4.1.2	R Development Core Team	https://www.R-project.org/
ImageJ	ImageJ	N/A
Flowjo10	Becton Dickinson & Company	RRID: SCR_008520
CaseViewer v2.4.0.119028	3DHISTECH	N/A
NDP.view2	Hamamatsu	N/A
Visiopharm v2022.11		N/A
SPSS26.0	SPSS Inc	N/A
GraphPad Prism 9	GraphPad Software Inc	RRID: SCR_002798
Other		
Corning® 6.5 mm Transwell® with 8.0 µm Pore Polycarbonate Membrane Insert	Corning	3422
Corning® 6.5 mm Transwell® with 3.0 µm Pore Polycarbonate Membrane Insert	Corning	3542

EXPERIMENTAL MODEL AND STUDY PARTICIPANT DETAILS

Human subjects

Three patients diagnosed with PCLM at PUMCH were enrolled in this study, which strictly followed the guidelines of the Ethics Committee of PUMCH (ethical approval number: 1-22PJ138). All patients did not receive any antitumor therapy before surgery, and all

provided written informed consent for sample collection and data analysis. All patients were in good physical condition and underwent surgery. All patients and their families had a strong desire for surgery. All patients had limited liver metastases, less than three, with low metastatic load, and tumor marker CA199 less than 1000 U/ml. The decision for the operations was made based on extremely careful preoperative assessment.

The retrospective information and used tumor tissue of PC patients with/without liver metastasis at the PUMCH from January 2020 to December 2023 were collected. All patients did not receive any antitumor therapy before surgery, and all provided written informed consent for sample collection and data analysis. The protocols were approved by the Ethics Committee of PUMCH. The specific information about the patients is shown in [Tables S1](#) and [S4](#).

Animal models

C57BL/6 mice and KPC mice were housed in the Peking Union Medical College specific pathogen-free animal facility at 20°C–22°C and 30%–70% humidity with a 12-h light/12-h dark cycle. Age- and sex-matched mice were used for all experiments. All experiments were performed under the approval of the Institutional Animal Care and Use Committee of PUMCH, and all experiments adhered to the guidelines of the Declaration of Helsinki and the Guiding Principles in the Care and Use of Animals.

Cells

HL-60, HEK-293 and MIA PaCa-2 cell lines were obtained from Procell (Wuhan, China). The Panc02 cell line was kindly provided by Dr. Lei You (Department of General Surgery, Peking Union Medical College Hospital, Beijing, China). Panc02, HEK-293 and MIA PaCa-2 cells were cultured in DMEM medium (Gibco) supplemented with 10% FBS and antibiotics (C0222, Beyotime). HL-60 cells were cultured in IMDM medium (Procell) with 20% FBS and antibiotics (C0222, Beyotime). Isolated neutrophils were cultured in RPMI-1640 medium (Procell) with 10% FBS and antibiotics (C0222, Beyotime). Neutrophil-like differentiated HL-60 (dHL-60) cells were induced by supplementing 1% DMSO in culture media of HL-60 for 6 days. All cell lines were cultured according to American Type Culture Collection protocols and regularly tested for *Mycoplasma* using the MycoBlue Mycoplasma Detector Kit (D101, Vazyme).

METHOD DETAILS

10x single-cell sequencing

For scRNA-seq, the cell suspension (300–600 living cells/µL, confirmed by Count Star) were loaded onto the Chromium single-cell controller using the Single Cell 3' GEM, Library & Gel Bead Kit V3.1 (10x Genomics, California, USA) and Chromium Single Cell B Chip Kit (10x Genomics, California, USA). Single-cell gel beads in the emulsion were generated according to the manufacturer's protocol. In short, single cells were suspended in PBS containing 0.04% BSA. Approximately 6,000 cells were added to each channel, with an estimated recovery of about 3,000 cells. Captured cells were lysed, then the released RNA was barcoded through reverse transcription in GEM reactions. Reverse transcription was performed on a S1000TM Touch Thermal Cycler (Bio-Rad) at 53°C for 45 min, followed by 85°C for 5 min, then held at 4°C. The cDNA was generated and amplified, then quality assessed using an Agilent 4200 (CapitalBio Technology, Beijing, China).

scRNA-seq data processing, quality control, and data visualization

Raw reads were processed to generate gene expression profiles using Cell Ranger v6.1.0 with default parameters. Scanpy v1.8.2 was used for quality control, dimensionality reduction, and clustering. Filtering criteria included cells with gene counts <200 or in the top 2% gene count, top 2% UMI count, and >10% mitochondrial content, with genes expressed in <5 cells excluded. After filtering, 47,587 cells were retained for the downstream analyses, with an average of 2,180 genes and 8,466 UMIs per cell. The raw count matrix was normalized by total counts per cell and logarithmically transformed into a normalized data matrix. The top 2,000 variable genes were selected by setting flavor = 'seurat'. PCA was performed on the scaled variable gene matrix, and the top 20 principal components were used for clustering and dimensional reduction. Cells were separated into many clusters using the Louvain algorithm and setting the resolution parameter at 1.2. Cell clusters were visualized using UMAP.

Cell type recognition with Cell-ID

Cell-ID is multivariate approach that extracts gene signatures for each individual cell and performs cell identity recognition using hypergeometric tests (HGTs). Dimensionality reduction was performed on the normalized gene expression matrix through multiple correspondence analysis, where both cells and genes were projected in the same low dimensional space. Then, a gene ranking was calculated for each cell to obtain the most featured gene sets of that cell. HGTs were performed on these gene sets against a brain reference from the SynEcoSys database, which contains distinctive genes for various cell types. The identity of each cell was determined as the cell type with the minimal HGT *p*-value. For cluster annotation, the frequency of each cell type was calculated in each cluster. The cell type with the highest frequency was used as the cluster's identity.

Cell malignancy estimation by scCancer

The InferCNV v1.20.0 was used to detect Copy Number Alterations (CNAs) in cancer cells. Endothelial cells were used as the baseline to estimate the CNAs of malignant cells. Genes expressed in more than 20 cells were sorted based on their loci on each chromosome.

The relative expression values were centered to 1, using a 1.5 standard deviation from the residual-normalized expression values as the ceiling. A slide window size of 101 genes was used to smoothen the relative expression on each chromosome and to remove the effect of gene-specific expression.

Differentially expressed gene (DEG) and pathway enrichment analysis

To identify DEGs, we used the Seurat FindMarkers() function based on the Wilcoxon rank-sum test with default parameters. The genes expressed in more than 10% of the cells in both compared groups and had an average log (Fold Change) value greater than 0.25 were selected as DEGs. To identify potential functions of cell types, GO enrichment analyses were used with the clusterProfiler v3.16.1. The protein-protein interaction networks of the DEGs were constructed by GENEMANIA software. The *p*-values <0.05 were considered statistically significant.

Monocle2

The cell differentiation trajectory of monocyte subtypes was reconstructed using Monocle2 v2.10.0. The top 2,000 highly variable genes were selected, and dimension-reduction was performed using DDRTree(). The trajectory was visualized using the plot_cell_trajectory() function.

RNA velocity

For RNA velocity, BAM files containing different cell clusters and the reference genome GRCh38 (hg38) were used with scVelo v0.17.17 in python with default parameters. The results were projected to the UMAP plot from Seurat clustering analysis for visualization consistency.

Cell-cell interaction (CCI) analysis: CellPhone DB

CCIs were predicted using known ligand-receptor pairs with Cellphone DB v2.1.0. The permutation number for calculating the null distribution of average ligand-receptor pair expression in randomized cell identities was set to 1000. Thresholding of individual ligand or receptor expression was performed using a cutoff value derived from the average log gene expression distribution across each cell type. Predicted interaction pairs with a *p*-values <0.05 and average log expression >0.1 were considered as significant and visualized in Cellphone DB.

UCell gene set scoring

Gene set scoring was performed using the UCell v1.1.0. UCell scores were based on the Mann-Whitney U statistics by ranking the query genes in expression level order in individual cells.

Transcription factor regulatory network analysis: pySCENIC

A transcription factor network was constructed by pyscenic v0.11.0 using scRNA expression matrix and transcription factors in AnimalTFDB. First, GRNBoost2 was used to predict a regulatory network with regulator and target co-expression. CisTarget was then applied to exclude indirect targets and search transcription factor binding motifs. Next, UCell was used for regulon activity quantification for every cell. Cluster-specific transcription factor regulons were identified according to Regulon Specificity Scores, and the activity of these regulons was visualized in heatmaps. In addition, prediction of transcription factors binding to target genes was based on JASPAR databases.

Survival analysis

Bulk RNA-seq transcriptomic data and clinic information were obtained from TCGA, ICGC and GEO database. Univariate and multi-variate Cox regression analyses were conducted based on the Neutrophils_S100A12 signature. Patients were stratified into high-signature and low-signature groups, and the optimal cut-off was determined using the ROC curve. The *p*-values calculated via the log rank test.

Spatial transcriptomics data processing and clustering

Tissue sections were generated from the collected patients' samples and tested on the machine after determining morphology. Spatial RNA-seq data from two 10X Visium capture areas, in which each contained 5,000 barcoded spots, were first processed by Space Ranger analysis software. The result matrix files were analyzed using the Seurat v4.0.1. During the standardized pipeline, feature counts for each spot were divided by the total counts for that cell, multiplied by the scale factor (1×10^6), and then log transformed using log1p. The top 2,000 highly variable genes from the Seurat object were selected by Seurat v4.0.1 using the FindVariableFeatures function (). These genes were used to perform PCA analysis and reduced the dimensions of the data to the top 20 principal components, followed by scaling and centering features in the dataset (ScaleData). The datasets could be visualized with reduced UMAP dimensions. Additionally, the FindNeighbours and FindClusters functions were used together to cluster the spots on Principal Component Analysis (PCA) space using the Shared Nearest Neighbor algorithm. The marker genes were then visualized with the FeaturePlot and SpatialFeaturePlot functions.

To optimize spatial clustering, BayesSpace v1.2.0 was applied for Spatial transcriptomics (ST) data. ST raw counts were pre-pressed with the spatialPreprocess() function with log-normalization and spatial variable genes selection. Spatial clustering was performed for the top 15 PCA components with the initial clustering method setting as kmeans. To identify the optimal number of clusters, we tested a sequence of cluster numbers. The number of clusters with a slope of negative log likelihood closest to 0 in qTune() analysis was selected for downstream analysis.

To estimate the significance of the overlap between ST genes of spatial clusters and cell type-specific genes from the scRNA-seq data, Metric for Intersected Analysis was used.

Immunohistochemistry (IHC)

Formalin-fixed, paraffin-embedded samples were obtained from the Department of Pathology of PUMCH. Routine H&E staining was performed, and the slides were scanned using CaseViewer (3DHISTECH). All tissue sections were dewaxed at 60°C for 2 h, followed by dimethylbenzene treatment. Different concentrations of ethanol were then used to hydrate the tissues. Antigen retrieval was performed with an EDTA buffer, then the catalase activity was blocked with 3% hydrogen peroxide. The sections were blocked with 5% BSA, followed by incubation with the primary antibodies at 4°C overnight. The next day, the sections were incubated with horseradish peroxidase-labeled secondary antibody at room temperature for 2 h. The histopathological images were examined by two experienced pathologists. NDP.view2 (Hamamatsu) and Visiopharm v2022.11 were used for image viewing and analysis. Tumor areas were manually defined using the NDP.view2, then scoring was performed in a blinded manner for all samples. The positive threshold was set between 0.4 and 0.9 according to the different indicators. We used the PANO 7-plex IHC kit (0004100100, Panovue) to perform multiplex IHC assay. Multispectral images were scanned with Axioscan 7.

Intrasplenic injection liver metastasis model

Experimental liver metastasis was performed by intrasplenic injection of 1×10^6 tumor cells into 6-week-old male C57BL/6 mice. At the indicated time point, luciferin emission imaging was performed using the PerkinElmer IVIS Spectrum to assess metastasis. All metastases were confirmed histologically, and the metastatic burden was calculated as the number of tumors multiplied by the tumor size.

For *in vivo* pharmaceutical inhibition of TGF- β , SM16 (HY-111482, MedChemExpress) was continuously intraperitoneally injected at a low dose of 15 mg/kg every three days^{52,53}; For *in vivo* pharmaceutical inhibition of NETs, Cl-amidine (S8141, Selleck) was continuously intraperitoneally injected at a dose of 20 mg/kg every two days; For *in vivo* neutrophil depletion, anti-mouse Ly6G (BE0075-1, BioXcell) was continuously intraperitoneally injected at a dose of 100 μ g; For *in vivo* SiNFE2, 10 nM SiNFE2 was injected via the tail vein three times a week. IgG2a isotype control (BE0085, BioXcell) serves as a non-reactive isotype-matched control for anti-mouse Ly6G (BE0075-1, BioXcell); SiNC acts as a negative control for SiNFE2; the dissolution reagent for Cl-amidine was used as a negative control for Cl-amidine. The dissolution protocol was performed following the manufacturer's instructions. The siRNAs used in this study were purchased by RiboBio Co., LTD (Guangzhou, China).

Immune cells isolation and flow cytometry

KPC mice were monitored for the emergence of liver metastases by 7T MRI (BioSpec 70/20USR). KPC mice or C57BL/6 mice were anesthetized, and the hepatic portal vein was exposed by dissection. Pancreas was minced and subjected to enzymatic digestion using (2 mg/mL collagenase IV, 100 μ g/mL DNase I, and 2 mg/mL dispase II) at 37°C for 30 min. Liver was perfused with predigestion (150 U Heparin sodium, 2 mmol/L EGTA, and 2 mg/mL dispase II) for internal digestion. Then, the tissues were carefully minced and external digested (2 mg/mL collagenase IV, 100 μ g/mL DNase I, and 2 mg/mL dispase II) for 30 min. The digestion was quenched by DMEM/F12 medium (Gibco) containing 10% fetal bovine serum (FBS) and filtered with 70 μ m Nylon mesh. Subsequently, the cell suspensions were purified through 30% Percoll density gradient centrifugation to isolate the desired cells. The collected mouse blood was lysed to remove red blood cells repeatedly following the manufacturer's instructions.

Single-cell suspensions were labeled with Fixable viability Stain 780 (565388, BD Biosciences) for 15 min and blocked with anti-mouse CD16/CD32 antibodies (553141, BD Biosciences) for 10 min. The fluorophore-conjugated antibodies were used and incubated for 30 min at room temperature in the dark. BD LSRIFortessa was used for flow cytometry. We use the MoFlo Astrios EQ for cell sorting and conduct *in vitro* experiments with freshly sorted cells.

In vitro pharmaceutical assays

SM16 is a kinase inhibitor that mainly targets ALK4/5, with only slight inhibitory activity against Raf or p38/SAPK2a pathways.⁵³ SB431542 primarily inhibits ALK4/5/7, without significant impact on other kinase pathways.⁵⁴ Due to the relatively high selectivity and specificity, SM16 and SB431542 are commonly used as effective inhibitors of the TGF- β signaling pathway. For pharmaceutical inhibition TGF- β , dHL-60 cells were treated with SM16 (HY-111482, MedChemExpress) at a dose of 10 μ M/mL or 20 μ M/mL for 24 h. To inhibit enhanced TGF- β signaling, dHL-60 cells/mouse neutrophils were pretreated with SB431542 for 30 min. To pharmaceutical stimulation of TGF- β signaling, dHL-60 cells/mouse neutrophils were stimulated with HumanKine recombinant human TGF- β (HZ-1011, Proteintech) at a dose of 5 ng/mL for 30 min. Mouse neutrophils were treated with TTS and boiled TTS for 30 min (from LM) or 60 min (from PT).

Luciferase reporter assay

To examine the transcriptional regulatory activity of NFE2 on PADI4, HEK-293 cells were transfected with the pGL3 Basic-PADI4-WT or pGL3 Basic-PADI4-Mut reporter together with the Renilla luciferase reporter internal control. To examine the transcriptional regulatory activity of SMAD3 on NFE2 or PADI4, HEK-293 cells were transfected with the pGL3 Basic-NFE2-WT or pGL3 Basic-PADI4-WT together with the Renilla luciferase reporter internal control. Lipofectamine 3000 (L3000001, Thermo Fisher Scientific) was employed for the transfection, and the subsequent detection of firefly and Renilla luciferase activities was carried out using the Dual Luciferase Reporter Assay System (E1910, Promega). The full-length plasmids were procured from GeneChem (Shanghai, China).

Suspension cell transfection assays

dHL-60 cells (2×10^6 cells) were mixed with 1 μg of plasmid expressing enhanced green fluorescence protein (EGFP) or 2 μg of small interfering RNA (siRNA) cocktails and transferred to the SF Cell Line 4D-Nucleofector X Kit S (V4XC-2024, Lonza). Freshly sorted mouse neutrophils (2×10^6 cells) from liver were transfected using the human monocyte nucleofection kit (VPA-1007, Lonza). After transfection, cells were resuspended in pre-warmed medium and rested in humidified 37°C/5% CO₂ incubator for 6 h before proceeding with subsequent experiments. Transfection was performed following the manufacturer's instructions. Transfection efficiency was monitored in each experiment by scoring the percentage of EGFP-positive cells by flow cytometry analysis. The siRNAs used in this study were purchased by RiboBio Co., LTD (Guangzhou, China). The target sequences of siRNA were listed in [Table S7](#).

Lentiviral infection

To achieve stable expression of luciferase, Panc02 cells were transfected with lentivirus (Ubi-MCS-firefly_Luciferase-SV40-neomycin). The shRNA targeting *Tgfb1* was packaged into lentiviral vector GV493 (hU6-MCS-CBh-gcGFP-IRES-puromycin). Stable Panc02 cell lines were established through lentiviral transduction following the manufacturer's protocol. After three days, cells were selected using medium containing 2 $\mu\text{g}/\text{mL}$ puromycin (HY-B1743A, MedChemExpress) or 800 $\mu\text{g}/\text{mL}$ G418 (ST081, Beyotime) and were maintained in medium containing 1 $\mu\text{g}/\text{mL}$ puromycin (HY-B1743A, MedChemExpress) or 200 $\mu\text{g}/\text{mL}$ G418 (ST081, Beyotime). Expression of TGF- β was determined by PCR and ELISA, and two cell lines (sh*Tgfb1*-1, sh*Tgfb1*-2) were selected for *in vivo* experiments. The lentiviruses were commercially obtained from Gene Chem (Shanghai, China). The target sequences of shRNA were listed in [Table S7](#).

Western blotting

The cells were lysed using RIPA Lysis Buffer (C1053-100, APPLYGEN) supplemented with protease inhibitor cocktail (AQ551, Aqlabtech), phosphatase inhibitor (P1260, APPLYGEN), and PMSF (ST505, Beyotime). The protein concentration was measured with the Enhanced BCA Protein Assay Kit (P0010, Beyotime). Total proteins were separated by SDS-PAGE on 10% gels and transferred to 0.45 μm polyvinylidene fluoride membranes. Then, 5% skim milk (AQ62321, Aqlabtech) was used to block the membranes for 2 h at room temperature. The membranes were then incubated with specific primary antibodies at 4°C overnight. After washing with Tris-buffered saline containing Tween 20, the membranes were then incubated with HRP-conjugated goat anti-mouse or anti-rabbit secondary antibodies (1:10000, Zsbio) and visualized using Super ECL Reagent (AQ529, Aqlabtech).

RNA extraction and quantitative real-time PCR

Total RNA was extracted from cultured cells using the RNA-Quick Purification Kit (Shanghai Yishan Biotechnology Co, Ltd, #ES-RN001), and complementary DNA synthesis was performed using the PrimeScript RT reagent Kit (Takara, #RR047A) according to the manufacturer's instructions. Quantitative real-time PCR was performed in triplicate using SYBR Green Master Mix (Applied Bio-systems, #A25742). ACTB was used as a housekeeping control, and the relative expression of messenger RNA was calculated using the $2^{-\Delta\Delta\text{CT}}$ method. The sequences of the primers used for quantitative real-time PCR were listed in [Table S7](#).

ELISA

The level of total TGF- β in mice tissue and cell culture supernatant were measured using the Mouse TGF-beta 1 ELISA Kit (RayBiotech, USA) according to the protocol of the manufacturer.

For tissue lysate supernatant preparation, LM from KPC mice with metastasis and normal tissue from the same liver region of KPC mice without metastasis were collected. In addition, adjacent pancreas (AP), PT, AL and LM from the same KPC mice with PCLM were also collected. Approximately 50 mg tissues were removed intact and washed with cold PBS. The tissue was soaked in cold PBS and mechanically sheared; the tissue supernatant was obtained by centrifugation at 12,000 g for 10 min after filtration.

For cell culture supernatant preparation, lentivirus-transfected cells were cultured using serum-free DMEM for 12 h. The DMEM medium (Gibco) was then collected, centrifuged at 1500 g for 15 min, and filtered through a 0.22 mm filter to obtain the cell culture supernatant.

In vitro indirect co-culture assays

After completion of pharmaceutical stimulation, dHL-60 cells/mouse neutrophils were washed twice with cold PBS. The washed dHL-60 cells/mouse neutrophils were resuspended in IMDM/RPMI-1640 medium (Percoll) and rested for 12 h. The medium was then collected, centrifuged at 1500 g for 5 min, and filtered through a 0.22 mm filter to obtain the conditioned medium.

MIA PaCa-2 cells/Panc02 cells were seeded in 96-well plates and cultured in the presence of conditioned medium from the control and pharmaceutical stimulation groups. The cell viability was assessed 48 h later using cell counting kit 8 (Dojindo, Japan). MIA PaCa-2 cells/Panc02 cells were loaded in the upper chamber of transwell plates (3422, Corning) and supernatants from the control or pharmaceutical stimulation group were added to the lower chamber. The plates were incubated at 37°C for 24 to 48 h. Migrated cells were stained with crystal violet (C0121, Beyotime) and counted in three random high-power fields under a microscope.

Neutrophil migration assay

Briefly, transwell inserts with 3- μ m pores and wells of a 24-well plate (3542, Corning) were coated with 2% BSA for 1 h at 37°C and washed twice with DPBS (14190144, Thermo Fisher SCIENTIFIC). Mouse neutrophils were pretreated with different concentrations of TGF- β or vehicle controls for 30 min while rotating at 37°C. 4×10^5 were then plated onto the transwell membranes in 200 μ L FBS-free RPMI-1640 medium (Percoll) and allowed to migrate toward RPMI-1640 medium (Percoll) containing 10% FBS for 2 h at 37°C. After 2 h, the number of cells that had migrated to the bottom chamber were counted using a hemocytometer, and the percentage of cells migrated was calculated. Similarly, different concentrations of TGF- β were added to RPMI-1640 medium (Percoll) containing 10% FBS in the lower chamber, and the migratory capacity of human neutrophils was tested by counting the number of cells that migrated to the lower chamber after 2 h at 37°C.

QUANTIFICATION AND STATISTICAL ANALYSIS

Statistical analysis

Student's t test, one-way ANOVA, Wilcoxon rank-sum test were used to compare differences. Survival curves were generated using the Kaplan-Meier method and compared with the Log rank test. All statistical analyses were performed using the statistical software package SPSS26.0 (SPSS Inc, Chicago, USA) and GraphPad Prism 9 (GraphPad Software Inc). The data shown are representative of at least three independent experiments. Data are presented as the mean \pm SEM. ns, not significant. * $p < .05$; ** $p < .01$; *** $p < 0.001$; **** $p < .0001$.